JOURNAL OF GEOPHYSICAL RESEARCH, VOL. 111, B09404, doi:10.1029/2005JB003976, 2006

Three-dimensional density model of the Nazca plate and the Andean continental margin

Andrés Tassara,[1,2] Hans-Jürgen Götze,[3] Sabine Schmidt,[3] and Ron Hackney[3]

Received 3 August 2005; revised 22 April 2006; accepted 1 June 2006; published 26 September 2006.

[1] We forward modeled the Bouguer anomaly in a region encompassing the Pacific Ocean (85°W) and the Andean margin (60°W) between northern Peru (5°S) and Patagonia (45°S). The three-dimensional density model that reproduces the gravity field is a continental-scale representation of density structure to 410 km depth that characterizes the mantle and crust of the oceanic Nazca plate, subducted slab and continental margin with a minimum number of bodies. We predefined the density of each body after studying the dependency of density on composition of crustal and mantle materials and pressure-temperature conditions appropriate for the Andean setting. A database of independent geophysical information constrains the geometry of the top of the subducted slab, locally the Moho of the oceanic and continental crusts and, indirectly, the lithosphere-asthenosphere boundary underneath the continental plate. Other boundaries, notably the intracrustal density discontinuity separating upper from lower crust below the continent, were not constrained and their geometry is the result of fitting the observed and calculated Bouguer anomaly during forward modeling. This contribution presents the model to the Andean geoscientific community and contains some tools, like a sensitivity analysis, that helps potential users of the model to interpret its results. We describe and discuss some of these results in order to illustrate the application of the model to the study of a wide range of phenomena (e.g., modification of oceanic plate structure by hot spots, shape of the subducted slab, thermal structure of the continental lithosphere, compensation mechanism and formation of orogenic relieve, causes of Andean segmentation).

Citation: Tassara, A., H.-J. Götze, S. Schmidt, and R. Hackney (2006), Three-dimensional density model of the Nazca plate and the Andean continental margin, *J. Geophys. Res.*, *111*, B09404, doi:10.1029/2005JB003976.

1. Introduction

[2] The Andean Cordillera is a continuous mountain chain along the western edge of South America that formed by a uniform process of oceanic subduction underneath a continental margin. After 200 Myr of convergence, this process has left a highly segmented margin that is characterized by systematic along-strike variations in topography, morphology, tectonics, basin distribution, volcanism, subduction geometry, deep lithospheric structure and geologic history [e.g., *Gansser*, 1973; *Jordan et al.*, 1983; *Isacks*, 1988; *Mpodozis and Ramos*, 1989; *Cahill and Isacks*, 1992; *Kley et al.*, 1999; *Gutscher*, 2002; *Jacques*, 2003; *Stern*, 2004]. In order to define a primary framework for discussion and to avoid the differences between previous definitions, we propose the following boundaries and nomenclature for continental-scale segmentation of the Andes (see inset of Figure 1a): northern (10°N–5°S), central (5°S–33.5°S), southern (33.5°–46.5°S) and austral (46.5°–56°S) Andes.

[3] The causes of this segmentation are not yet understood. Several authors argue that the correlation between features of the oceanic Nazca plate at the trench (age, subduction of ridges), along-strike changes in the shape of the subducted slab and boundaries between the Andean segments (Figure 1a) means that this segmentation is primarily controlled by the current configuration of the subducting plate [e.g., *Jordan et al.*, 1983; *Pilger*, 1984; *Pardo-Casas and Molnar*, 1987; *Gutscher et al.*, 2000; *Ramos et al.*, 2002; *Yáñez et al.*, 2001, 2002; *Yáñez and Cembrano*, 2004]. However, compared with the timescale over which the configuration of the oceanic plate changes (10^6–10^7 years), the segments and their boundaries are longstanding (10^8 years) geological features of the Andean margin [e.g., *Gansser*, 1973; *Mpodozis and Ramos*, 1989; *Mégard*, 1984; *Kley et al.*, 1999]. This observation suggests that the old structure of the continent should also play a role in controlling the fate of the Andean margin and the maintenance of its segmentation.

[4] The evaluation of this hypothesis requires knowledge of the compositional structure of the convergence system at continental scales. We have tried to fulfil this requirement by forward modeling the Bouguer anomaly for the central

---

[1] Institut für Geologische Wissenschaften, Freie Universität Berlin, Berlin, Germany.

[2] Now at Departamento de Geofísica, Facultad de Ciencias Físicas y Mateméticas, Universidad de Chile, Santiago, Chile.

[3] Institut für Geowissenshaften, Christian-Albrechts-Universität zu Kiel, Kiel, Germany.

0148-0227/06/2005JB003976$09.00

and southern Andes between 5° to 45°S and 60° to 85°W (Figure 1a). The main aim was to produce a model that (1) describes the three-dimensional (3-D) density structure of the continental lithosphere, the Nazca plate and the subducted slab down to 410 km depth, and (2) can be used to analyze first-order structural and compositional variations along the continental margin. This goal was achieved without considering the details of regional and local structures, but by producing a model that contain valuable information at the scale of the entire Andean margin. After a revision of the Andean geotectonic framework, data and methods, we present the 3-D density model and discuss its main features and implications for the geodynamic processes acting along the western margin of South America.

2. Andean Geotectonics

[5] The first-order geotectonic elements of the Nazca plate and the South American continent are shown in Figure 1a. The age of the oceanic plate [*Müller et al.*, 1997] along the Peru-Chile trench increases from 0 Myr at the triple junction with the Antarctic and South American plates (46.5°S, south of the area considered in this study) to a maximum of ~48 Myr around 20°S. North of this latitude, the continental margin changes its orientation from NNE to NW, a feature known as the Arica Bend. The age of the oceanic lithosphere at the trench decreases to ~28 Myr at 5°S. Along-strike jumps in age are associated with fracture zones that are recognizable as bathymetric lows with a general azimuth of ~70°. This is 10° less than the average convergence direction defined by GPS measurements [e.g., *Kendrick et al.*, 2003]. Bathymetric highs correspond to aseismic ridges (i.e., Nazca, Juan Fernández and Iquique) and to the active spreading center of the Chile Rise.

[6] Contours of the depth to the subducted slab, from data available with the Generic Mapping Tools [*Wessel and Smith*, 1998], are plotted in Figure 1a and show two segments of relatively flat subduction at intermediate depths (70–150 km) below Peru (5°–15°S) and Argentina (28°–33°S). The spatial correlation with the subduction of the Nazca ridge at 15°S and the Juan Fernández ridge at 33°S suggests a causative relationship with the development of these flat slab segments [e.g., *Gutscher et al.*, 2000; *Yáñez et al.*, 2002]. Elsewhere, the slab subducts with a dip of 25–35° to ~200 km depth, increasing at greater depths.

[7] Figure 1a also shows the position of modern volcanoes and morphotectonic units forming the continental margin. On the basis of the propositions of *Jordan et al.* [1983], *Mégard* [1984], *Mpodozis and Ramos* [1989], *Allmendinger et al.* [1997], and *Kley et al.* [1999], these morphotectonic units have been redrawn using a GIS-based analysis of digital topography and digital geological databases of South America [*Schobbenhaus and Bellizzia*, 2001], Argentina [*Servicio Nacional de Geológica Minero Argentina*, 1998] and Chile [*Servicio Nacional de Geologia y Mineria*, 2003]. The Andean forearc is dominated by the Coastal Cordillera. Along segments with steep subduction, this unit is separated from the high internal cordilleras by forearc basins (Intermediate Depression and central Valley). Some uplifted Coastal Plains form prominent peninsulas (e.g., Mejillones and Arauco) that disturb the otherwise smooth coastline. The offshore forearc is very steep between the points where the Nazca and Juan Fernández ridges subduct, but has a more subtle bathymetry and contains submarine basins to the north [e.g., *Clift et al.*, 2003; *Krabbenhöft et al.*, 2004] and south [e.g., *Bangs and Cande*, 1997] of this area.

[8] The central Andes comprise a huge mountain range with elevations above 3500 m covering an area of ~800,000 km^2. The morphology is dominated by the Altiplano-Puna plateau that has a maximum width of ~400 km at 18.5°S. North and south of the plateau, the high cordilleras narrow to less than 200 km width. This narrowing correlates with a decrease in Neogene crustal shortening [e.g., *Isacks*, 1988; *Kley et al.*, 1999], which itself is related to systematic changes in the deformation style of the foreland: thin skinned along the Sierras Subandinas, thick skinned along the Santa Barbara System and the northern Eastern Cordillera, and basement uplift along the Sierras Pampeanas and Peruvian uplifted blocks [e.g., *Kley et al.*, 1999]. The absence of asthenospheric mantle above flat slab segments precludes the occurrence of arc magmatism and hence the Central Volcanic Zone (CVZ) of the Andes is restricted to the Western Cordillera between 15° and 28°S.

Figure 1. Geotectonic setting (a) and Bouguer anomaly (b) for the studied area. Inset shows the study area (rectangle with bold lines) and continental-scale segmentation of the Andean continental margin. (a) Andean geotectonic setting on a digital elevation map (http://www.ngdc.noaa.gov/mgg/gebco). White lines in the offshore region are isochrones of the Nazca plate [*Müller et al.*, 1997] with ages in million of years, names in capitals denote aseismic ridges and the active spreading center of the Chile Rise, and names in minuscule denote fracture zones. In the onshore region, white dotted lines with numbers are isodepths (in km) of the subducted slab from data available with GMT software package [*Wessel and Smith*, 1998], triangles are active volcanoes from the Smithsonian Institute database (http://www.volcano.si.edu/gvp/world), black lines depict boundaries of morphotectonic units as modified after references cited in the text: cpl, Coastal Plains; pub, Peruvian uplifted blocks; cc, Coastal Cordillera; id, Intermediate Depression; cv, Central Valley; dc, Domeyko Cordillera; wc, Western Cordillera; fc, Frontal Cordillera; ppc, Principal Cordillera; ab, Atacama Basin; ap, Altiplano; pn, Puna; pc, Precordillera; ec, Eastern Cordillera; sp, Sierras Pampeanas; ssa, Sierras Subandinas; sbs, Santa Barbara System; pgc, Patagonian Cordillera; srb, San Rafael Block; ns, Neuquén System; npm, North Patagonian Massif. (b) Bouguer anomaly map of the study region with contours every 100 mGal. Dots in the onshore region depict the location of land gravity stations (see text for data description). Lines are the 43 vertical cross sections from which the three-dimensional density structure of the model is triangulated. Thick lines coincide with fracture zones from Figure 1a and correspond to cross sections dividing the density structure of the oceanic plate and subducted slab in the seven segments labeled with roman numbers I to VII.

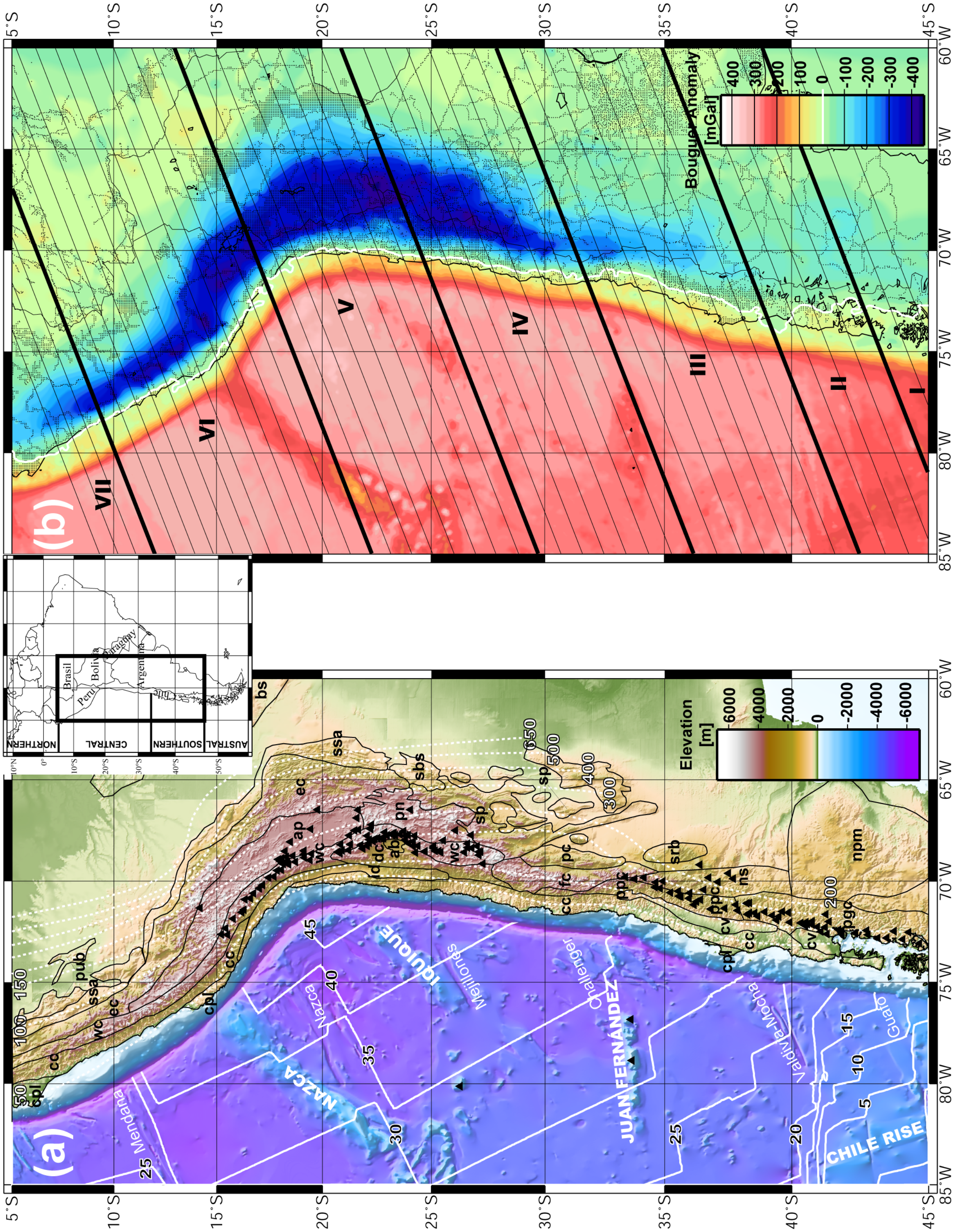
(a)
(b)
5°S
10°S
15°S
20°S
25°S
30°S
35°S
40°S
45°S
85°W
80°W
75°W
70°W
65°W
60°W
Mendana
NAZCA
Nazca
Iquique
Mejillones
Challenger
JUAN FERNÁNDEZ
Valdivia-Mocha
Guafo
CHILE RISE
5
10
15
20
25
30
35
40
45
50
100
150
200
300
400
500
650
cpl
cc
wc
ec
ssa
pub
ap
ab
dc
pn
sb
sbs
sp
pc
fc
ppc
srb
ns
cv
pgc
npm
bs
Elevation [m]
6000
4000
2000
0
-2000
-4000
-6000
NORTHERN
CENTRAL
SOUTHERN
AUSTRAL
Brasil
Peru
Bolivia
Paraguay
Argentina
Chile
10°N
0°
10°S
20°S
30°S
40°S
50°S
I
II
III
IV
V
VI
VII
Bouguer Anomaly [mGal]
400
300
200
100
0
-100
-200
-300
-400

Figure 1

[9] The boundary between the central and southern Andes at 33.5°S is a major tectonic transition [e.g., *Yáñez et al.*, 2002] bounding almost all the morphotectonic units exposed in this region. South of this latitude, elevations higher than ~4000 m decrease gradually along the Principal Cordillera to less than 2000 m in the Patagonian Cordillera. This decrease also correlates with north-south variations in the Neogene tectonic style. Basin inversion along the Principal Cordillera and thick-skinned foreland tectonics along the Neuquén System are linked to trench-oblique structures [*Godoy et al.*, 1999; *Charrier et al.*, 2002; *Cobbold and Rossello*, 2003]. These styles change south of 38°S to trench-parallel, dextral strike-slip along the Liquiñe-Ofqui Fault Zone (LOFZ) with dominant forearc extension and little shortening recorded along the Patagonian Cordillera and the North Patagonian Massif [e.g., *Diraison et al.*, 1998; *Lavenu and Cembrano*, 1999; *Folguera et al.*, 2004]. The steep subduction of the oceanic slab drives the mantle magmagenesis feeding the Southern Volcanic Zone (SVZ). The northern part of the SVZ forms the top of the Principal Cordillera, whereas the southern SVZ (south of 39°S) builds the western central part of the Patagonian Cordillera and is genetically related to the LOFZ [*Hervé*, 1994; *López-Escobar et al.*, 1995; *Cembrano et al.*, 1996].

3. Bouguer Anomaly

[10] Offshore Bouguer anomalies were computed from the KMS01 satellite-derived free-air anomaly database (*Andersen and Knudsen* [1998], http://geodesy.spacecenter.dk/GRAVITY) by applying a correction using digital bathymetric data (http://www.ngdc.noaa.gov/mgg/gebco) on a 2’ grid and replacing the water layer with material of density 2.67 Mg/m^3. Onshore gravity data for the South American continent have been compiled, homogenized and processed by the Escola Politecnica Universidade de São Paulo (Brazil). The database was provided by D. Blizkow (personal communication, 2003) in the framework of a cooperation agreement with the German Collaborative Research Centre SFB267 “Deformation Processes in the Andes” (hereinafter referred to as SFB267). We used the Bouguer anomaly of circa 20,000 stations from this database that cover the study area (dots in Figure 1b). *Marchenko* [2006], who exploited these data to compute a geoid model for the continent, estimate an average error in the onshore free-air anomaly of ~10 mGal. We assume that the further reduction to the Bouguer anomaly has expanded this error to an average uncertainty of ±20 mGal.

[11] Combining both databases, we generated the Bouguer anomaly map of Figure 1b. It shows a negative anomaly less than −200 mGal associated with the high cordilleras of the central Andes. This anomaly decreases locally to less than −400 mGal along portions of the Western Cordillera. A minimum of about −450 mGal is located around the boundary between the Altiplano and Puna. Along the southern Andes, the Bouguer anomaly is greater than −200 mGal and increases to the south. South of 38°S, the anomaly is no longer correlated with the cordilleras and its minimum (about −120 mGal) is located in the North Patagonian Massif. The 0 mGal contour coincides with the coastline along the Peruvian forearc, whereas in Chile it is shifted landward. This is more obvious south of 25°S and particularly along the southern Andes, where this contour follows the limit between the Coastal Cordillera and the Central Valley. Positive Bouguer anomalies are observed along the Andean foreland between 38° to 25°S and north of 15°S. They also dominate the offshore gravity field. The trench axis correlates with the 200 mGal contour and a strong positive gradient to the west. (Hereafter the terms very short, short, intermediate and long wavelengths are used for wavelengths <100 km, 100–300 km, 300–1000 km, and >1000 km, respectively (see Figure 2). Maximum Bouguer anomalies of ~350 mGal are observed together with less positive anomalies in patches of very short wavelength along the southwestern limit of the Nazca ridge. In general, oceanic ridges and fracture zones are characterized by regions of positive anomalies that are less pronounced than in their surroundings. Segments of oceanic lithosphere separated by fracture zones show maximum Bouguer anomalies along an outer rise west of the trench and a general increase in the magnitude of the anomaly from the north and south toward a region between the Nazca and Iquique ridges. This spatial variation is positively correlated with the age of the Nazca plate.

4. The 3-D Density Model

[12] Forward modeling of the Bouguer anomaly was performed using the IGMAS modeling software (Interactive Gravity and Magnetic Application System; see http://www.gravity.uni-kiel.de/igmas). The modeling software [*Götze*, 1984; *Götze and Lahmeyer*, 1988; *Schmidt and Götze*, 1998; *Breunig et al.*, 2000] makes use of an interoperable 3-D Geoinformation System (IOGIS) and its functionality. The model is formed by three-dimensional bodies that are constructed using polyhedra whose geometry is predefined by the user on a series of parallel vertical cross sections. Density values for the modeled bodies are also defined prior to the gravity modeling. By iteratively changing the geometry of the initial structure in accordance with the available constraining data incorporated in the IOGIS, the user eventually converges to the optimal fit between the observed Bouguer anomaly and the anomaly produced by the modeled 3-D density structure. This modeled anomaly is calculated from the density contrast between the modeled bodies and a simple background reference model. Thus the design of a 3-D density model in IGMAS incorporates three important decisions: the definition of the initial structure, the selection of density values for the bodies forming the model and the choice of a reference model. The rationale, data and procedures allowing these decisions to be made are described below.

4.1. Initial Model Structure

[13] The correlation between offshore Bouguer anomaly and Nazca plate age suggests that the density structure of the oceanic lithosphere is controlled by age discontinuities associated with fracture zones. Therefore we defined the vertical cross sections of the model in a direction parallel to them. Figure 1b shows the 43 sections forming the model. The sections are separated by 1° in latitude, have a length of ~3000 km and a depth of 410 km. Bold lines in Figure 1b are profiles coinciding with the six first-order fracture zones labeled in Figure 1a. In the model, segments of the oceanic

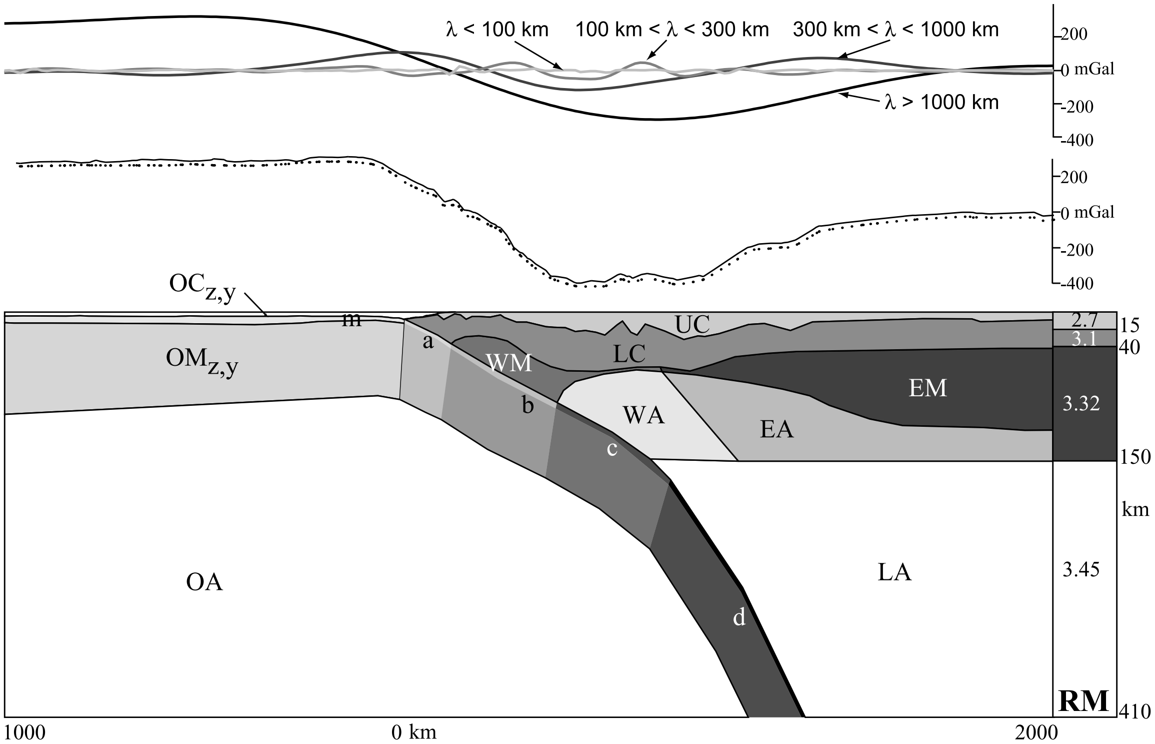

Figure 2. (bottom) One of the vertical cross sections showing the lateral (3000 km) and downward (410 km) extension of the model, and its general density structure with ~2 times vertical exaggeration. Right column labeled RM represents the reference model with the depth to density discontinuities and density values in Mg/m^3. Abbreviations of model bodies and their densities are defined in Table 1. See text for description. (middle) Observed Bouguer anomaly along this sections in bold line and Bouguer anomaly calculated from the density model in dotted line. They are shifted in some mGal in order to note the good fit between them. (top) Decomposition of the observed Bouguer anomaly after filtering to show the very short ($\lambda < 100$ km), short ($100 < \lambda < 300$ km), intermediate ($300 < \lambda < 1000$ km), and long ($\lambda > 1000$ km) wavelength components of the gravity field, as defined in the text.

lithosphere and the slab with distinctive density structure are in contact across these fracture zones. The resulting seven segments are labeled with roman numbers in Figure 1b.

[14] Figure 2 shows one of the cross sections as an example of the structure used to construct the model. This structure is simplified with respect to the complexity expected for subduction zones, but it is sufficient to describe the density structure of the convergence system at continental scales. The oceanic plate and slab are formed by a one-layer crust ($OC_{z,y}$) overlying a mantle lithosphere body ($OM_{z,y}$). The suffixes z and y are assigned specific values that aid the identification of each body in the model. The suffix z is equal to m for the marine part of the oceanic plate and a to d for the subducted parts of the slab (Figure 2). This division allows for downward densification of the slab. The suffix y takes values between I and VII along the strike of the study area (Figure 1b). The oceanic plate and slab are underlain by one body representing the asthenospheric mantle (OA in Figure 2).

[15] The continental plate is formed by a two-layer crust (UC and LC in Figure 2) overlying mantle lithosphere. The crustal structure is unrealistic because it does not account for the complex vertical stratification of the crust observed worldwide [e.g., *Christensen and Mooney*, 1995], nor for the lateral variation of crustal density that is very likely in a region extending over more than 4000 km that is characterized by complex surface geology. Note, however, that our intention is to use the depth to the intracrustal density discontinuity (ICD) separating upper and lower crust as a proxy for this complex density structure.

[16] The continental mantle lithosphere is formed by two bodies whose boundary is located underneath the easternmost active volcano observed within 50 km of each modeled section. The eastern lithospheric body (EM in Figure 2) represents the cold and dense mantle below the Andean foreland and shield regions. The western lithosphere (WM in Figure 2) should be less dense because it underlies the hot volcanic arc and is presumably hydrated underneath the forearc region. Below the lithosphere-asthenosphere boundary (LAB), asthenosphere shallower than 150 km is also formed by two bodies (WA and EA in Figure 2). These bodies attempt to represent the expected gradual decrease in asthenospheric density toward the volcanic arc produced by high temperatures and hydration of the wedge. The subcontinental mantle below 150 km depth is represented by one body of constant density (LA in Figure 2).

4.2. Reference Density Model

[17] We use a horizontally stratified, four-layer reference model that is homogeneous along the entire study region and typifies the density variations with depth in a column of average continental lithosphere. This is represented by the right column RM in Figure 2. The reference model has an

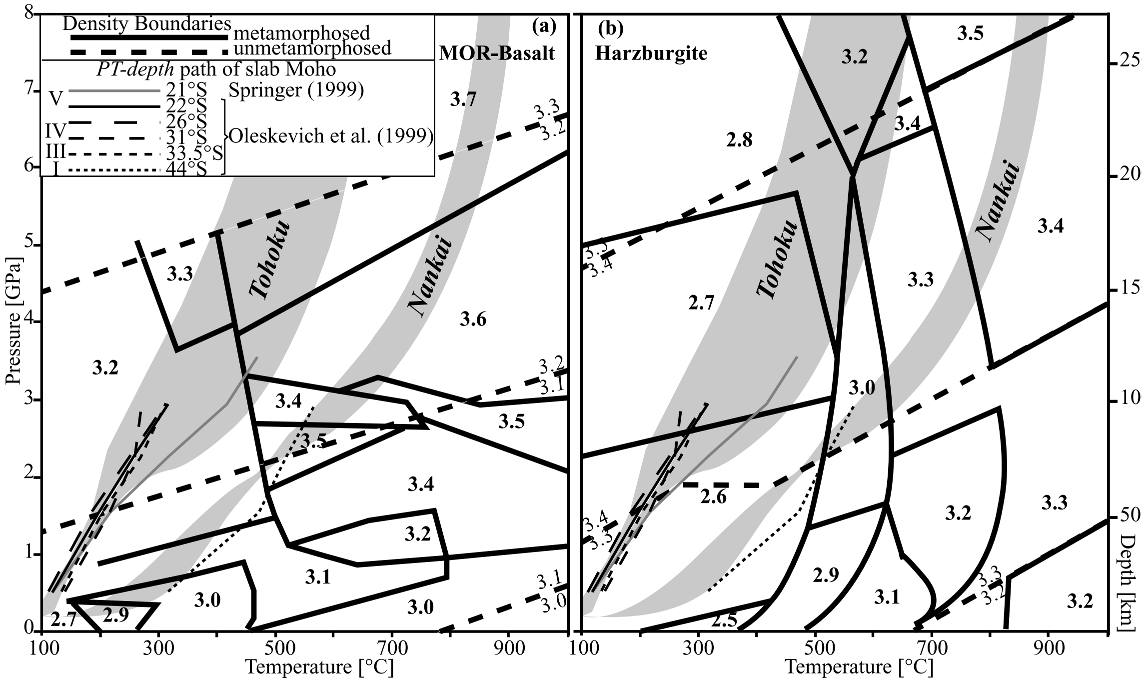

Figure 3. Pressure(depth)-temperature diagrams and boundaries of density fields associated with metamorphic facies for (a) MOR basalt and (b) harzburgite, after *Hacker et al.* [2003a]. Density boundaries are shown by thick lines, bold for metamorphosed rocks and segmented for unmetamorphosed rocks, with density values in Mg/m^3. Thin lines are PT-depth paths of oceanic Moho for some Andean profiles proposed by *Springer* [1999] and *Oleskevich et al.* [1999]. Grey regions labeled Tohoku and Nankai are after *Hacker et al.* [2003a].

ICD at 15 km and Moho at 40 km, consistent with the compilation of refraction seismic profiles of *Christensen and Mooney* [1995]. In Appendix A, we summarize our analysis of the thermal and density structure of the mantle. This shows that for a heat flow of 50 mW/m^2 along the studied shield region [*Hamza and Muñoz*, 1996; *Springer and Förster*, 1998], the depth to the LAB should be 150 km, the value that we selected for the reference model.

[18] The densities of each layer of the reference model are also shown in Figure 2. Following the petrophysical analysis of *Tassara* [2006], a density of 2.7 Mg/m^3 characterizes a crystalline upper crust formed by granites with 73 wt % SiO$_2$. The same analysis suggests that below 20 km depth, the lower crust can be effectively characterized by a density of 3.1 Mg/m^3. This is high compared with values of 2.8–3.0 Mg/m^3 typically assumed by gravity modelers [e.g., *Berrocal et al.*, 2004; *Mishra et al.*, 2004; *Zeyen et al.*, 2005], but it has also been selected by some authors to typify deep levels of the continental crust [e.g., *Ebbing et al.*, 2005; *Kozlovskaya et al.*, 2004]. For a lower crustal layer of "normal" thickness (i.e., located between 15 and ~35–40 km depth), *Tassara* [2006, Figure 2] indicates that a value of 3.1 Mg/m^3 represents the average density of an anhydrous gabbro crystallized from a calcalkaline basaltic-andesite to basaltic magma, or a more basic but hydrated mafic amphibolite. If the lower crust were buried to greater depths (50 to 70 km, like in the Andean crustal roots), this density is representative of metaigneous rocks with an andesite to basaltic-andesite composition.

[19] The density selected for the reference mantle lithosphere is 3.32 Mg/m^3. As shown in Figure A2b, this value is an average of those expected for a continental harzburgite with surface heat fluxes that are normal for shield regions (45–55 mW/m^2). A density of 3.45 Mg/m^3 for the sublithospheric mantle in the reference model is an average of values computed in Appendix A for a pyrolitic mantle along an adiabatic thermal gradient between 150 km and the bottom of the model at 410 km depth.

4.3. Selection of Density Values for Modeled Bodies

4.3.1. Nazca Plate

[20] Figure 3 summarizes the density values calculated by *Hacker et al.* [2003a] for metamorphosed and fresh mid-ocean ridge (MOR) basalts (Figure 3a) and harzburgite mantle (Figure 3b) for temperatures between 100° and 1000°C and pressures up to 8 GPa (~270 km depth). At near-seafloor conditions (bottom left corner of Figure 3a), fresh oceanic crust would have a density of 3.1 Mg/m^3, whereas its fully hydrated counterpart shows a reduced density of 2.7 Mg/m^3. The density of 3.05 Mg/m^3 selected for the oceanic crust of the reference model and segments III to VII of the Nazca plate (see selected densities in Table 1) implies a mixture of 85% fresh basalts and gabbros and 15% fully metamorphosed basalts that is consistent with seismic findings worldwide [e.g., *Carlson and Miller*, 2004]. This relatively high density is adequate for the basalt- and gabbro-bearing seismic layers 2 and 3 forming most of the oceanic crust. Note that in the calculation of this average density we do not consider the sedimentary seismic layer 1, because the incoming Nazca plate normally shows only a thin (<300 m) layer of pelagic sediments in seismic profiles [e.g., *Bangs and Cande*, 1997; *Flüh et al.*, 1998; *Krabbenhöft et al.*, 2004].

Table 1. Densities Selected for the Bodies Forming the 3-D Model[a]

	Oceanic Plate and Subducted Slab										Continental Plate				Asthenosphere			
	m		a		b		c		d									
Segment	OC	OM	OC	OM	OC	OM	OC	OM	OC	OM	UC	LC	WM	EM	OA	LA	WA	EA
I	2.98	3.26	2.98	3.26	3.25	3.30	3.35	3.38	3.55	3.5	2.7	3.1	3.24	3.32	3.41	3.45	3.31	3.35
II	3.00	3.30	3.00	3.30	3.2	3.33	3.3	3.4	3.55	3.5								
III	3.05	3.33	3.05	3.33	3.2	3.36	3.3	3.4	3.55	3.5								
IV	3.05	3.34	3.05	3.34	3.2	3.36	3.3	3.4	3.55	3.5								
V	3.05	3.355	3.05	3.355	3.2	3.37	3.3	3.4	3.55	3.5								
VI	3.05	3.35	3.05	3.35	3.2	3.36	3.3	3.4	3.55	3.5								
VII	3.05	3.34	3.05	3.34	3.2	3.36	3.3	3.4	3.55	3.5								

[a] Densities are in Mg/m^3. Abbreviations are I–VII, along-strike segments of the oceanic plate and subducted slab; m, marine part of the oceanic lithosphere; a–d, downward parts of the slab; OC, oceanic crust; OM, oceanic mantle lithosphere; UC, upper continental crust; LC, lower continental crust; WM, western continental mantle lithosphere; EM, eastern continental mantle lithosphere; OA, oceanic asthenosphere; LA, lower continental asthenosphere; WA, western continental asthenosphere; EA, eastern continental asthenosphere.

The reduction of the crustal density for the two southernmost segments (I and II, Table 1) is necessary for achieving a fit with the observed Bouguer anomaly near the trench axis. This reduction suggests either an intrinsically low crustal density, consistent with these segments being created at the slow spreading Chile Rise [*Henstock and Thompson*, 2004], or the existence of cracks that are still open and filled with seawater because the relatively young age of these segments precludes their closure [e.g., *Carlson*, 2004].

[21] Information summarized in Figure A2a, together with the age distribution of the Nazca plate [*Müller et al.*, 1997], was used to initially fix the thickness and density of the oceanic mantle lithosphere at the trench for each of the seven segments forming the Nazca plate in the model. However, the final densities selected for each body were fine tuned during the modeling in order to fit the observed long-wavelength Bouguer anomaly near the trench axis. The final density values for each segment are shown in Table 1.

4.3.2. Subducted Slab

[22] The densification of the slab with depth is the result of metamorphic reactions occurring in the oceanic crust and mantle as they are exposed to high temperatures and pressures during passage toward the deep mantle [e.g., *Kirby et al.*, 1996; *Peacock and Wang*, 1999; *Hacker et al.*, 2003a]. Understanding these reactions and their effect on the subducted slab density is restricted by the incomplete knowledge of the thermal structure of the Andean subduction zone. *Springer* [1999] and *Oleskevich et al.* [1999] proposed two-dimensional temperature profiles along some regions of the Andean forearc. From these profiles, we have extracted the (P)T-depth path of the slab Moho and plotted them in the diagrams of Figure 3. This information was used to gain insights into the probable changes in slab density with depth and to select the density values for crustal and mantle bodies of the slab segments a to d (Figure 2 and Table 1). In particular, it can be observed (Figure 3) that for relatively old segments of the Nazca slab (III to V; 33.5°S to 21°S), the PT-depth paths down to 100 km depth are very similar to each other and also to that of the Pacific slab subducting along the Tohoku trench. For these slabs, a relatively smooth increase in density is expected with depth, in contrast to the young and warm slab subducting at 44°S (segment I), which is comparable to the Philippine slab below Nankai. The high temperatures reached at shallow depths in these subduction zones imply an important increase in density at depths less than 100 km due to enhanced dehydration, mostly of the oceanic crust. Without a better understanding of the thermal structure along the Andean subduction zone, we consider the proposed density structure of the slab (Table 1) as a rough, but acceptable, first approximation.

4.3.3. Continental Margin

[23] Along the entire study region the continental crust is formed by two layers whose densities remain unchanged with respect to the values selected for the reference model, i.e., 2.7 Mg/m^3 for the upper crust and 3.1 Mg/m^3 for the lower crust. The expected spatial variation of the crustal density structure with respect to the reference model, mostly caused by lateral changes in compositional structure and thermal conditions within the crust [*Tassara*, 2006], is represented in this modeling by variations in the depth of the intracrustal density discontinuity (ICD). Owing to the high density value selected for the lower crust, the ICD is the most prominent density discontinuity below the continent and a large portion of the Bouguer anomaly will be absorbed by changing its geometry. In the discussion, we analyze the implications of using this density structure and the potential modifications of the resulting model produced by reducing the lower crustal density.

[24] The eastern mantle lithosphere (EM in Figure 2 and Table 1) maintains a density of 3.32 Mg/m^3, as in the reference model. Considering the information summarized in Appendix A, the selected density for the western mantle lithosphere body (WM in Figure 2 and Table 1) is 3.24 Mg/m^3. This value accounts for the very high heat flow observed along Andean volcanic arcs [*Henry and Pollack*, 1988; *Hamza and Muñoz*, 1996; *Springer and Förster*, 1998]. This body also underlies the forearc region, which is colder than the arc, but is affected by the extensive hydration likely to be caused by water liberated from the subducting slab. For the range of depths (30 to 100 km) and temperatures (150° to 600°C) expected for the Andean mantle forearc [e.g., *Oleskevich et al.*, 1999], Figure 3b predicts that a fully hydrated, serpentinized harzburgite should have an average density near 2.7 Mg/m^3, whereas a fresh harzburgite would have a density of 3.35 Mg/m^3. The selected value of 3.24 Mg/m^3 implies a mixture of 20% serpentinized harzburgite and 80% fresh harzburgite. These relative proportions are consistent with the percentage of serpentinization of the mantle forearc deduced from seismic studies worldwide [*Carlson and Miller*, 2003].

[25] The difference between lithosphere and asthenosphere in our model is both compositional and thermal. The lithosphere is thought to be composed by depleted

harzburgites whose density decreases toward the LAB along a conductive thermal gradient. In contrast, the asthenospheric bodies between the continental LAB and the reference depth of 150 km are formed by a fertile and hence dense lherzolite whose density increases downward along an adiabatic gradient. In this context, the asthenospheric bodies WA and EA (Figure 2) have an average density that is higher than the overlying lithosphere (Figure A2b), contrary to the common idea derived from the existence of a seismic low-velocity zone (LVZ) at the base of some continental plates [*Turcotte and Schubert*, 2002]. As shown in Figure A2b, the density of 3.35 Mg/m^3 selected for the eastern asthenosphere body is an average of the values expected for a fertile lherzolite and heat fluxes lower than 70 mW/m^2. The western asthenosphere below active volcanic zones, where heat flow is higher than 75 mW/m^2 [*Hamza and Muñoz*, 1996; *Springer and Förster*, 1998], can be represented by a density of 3.31 Mg/m^3, slightly lower than for the reference lithospheric mantle. This implies that this body has a negative density contrast producing a mass deficit in the model that can intuitively be associated with the seismic mantle LVZ.

5. Geometry of Density Discontinuities and Their Constraints

5.1. Oceanic Plate

[26] The oceanic crustal thickness was initially fixed to 7 km, the average global value [*White et al.*, 1992; *Bown and White*, 1994]. During modeling, the oceanic Moho was adjusted to match the local constraints given by refraction seismic profiles for some regions near the trench axis (Figure 4) and mostly by fitting the short- to intermediate-wavelength Bouguer anomaly along the modeled cross sections.

[27] For each segment forming the Nazca plate, our model represents the oceanic mantle lithosphere with one body whose thickness and density were initially forced to correspond with the age-predicted value at the trench axis. These predicted values were computed as described in Appendix A using the Nazca age grid of *Müller et al.* [1997]. In order to fit the intermediate- to long-wavelength Bouguer anomaly, these initial values were then optimized for an area near the trench axis. Figure A2a shows that a decrease in Nazca ages west of the trench implies a reduction in the age-predicted LAB depth in that direction and also a subsequent decrease in the average lithospheric density with respect to the value at the trench. This is the result of hotter thermal conditions for younger plates. Therefore a westward increasing lithospheric mass deficit with respect to the density structure at the trench can be predicted by the half-space cooling model. This is consistent with the offshore Bouguer anomaly that decreases toward the west (Figure 1b). With only one body of constant density representing the oceanic lithosphere in the model, we reproduce this pattern by replacing westward increasing amounts of dense sublithospheric mantle by lighter lithospheric material to fit the long-wavelength Bouguer anomaly.

5.2. Subducted Nazca Slab

[28] The Moho and upper surface of the slab have been imaged by reflection and refraction seismic profiles along some regions of the forearc. Receiver function studies also locally image the slab Moho. From the references listed in Figure 4, we digitized the depth to these discontinuities and included them in the model. This information was combined with hypocenters recorded by local seismic networks (as referenced in Figure 4) and complemented with seismicity registered at teleseismic distances and recorded in the USGS NEIC catalogue (http://neic.usgs.gov/neis/epic/), the "Centennial Global Earthquake Database" (http://www.geonavi.com/eric/HotNews/eqDB.html) and in data described by *Engdahl et al.* [1998]. To locate the upper surface of the slab, the digitized seismic images and the seismicity associated with the Wadati-Benioff zone within 50 km of each modeled cross section were considered. Selected profiles of the global tomography model of *Villaseñor et al.* [2003] were used to constrain the geometry of the slab at depths greater than 200 km, where seismicity is generally scarce.

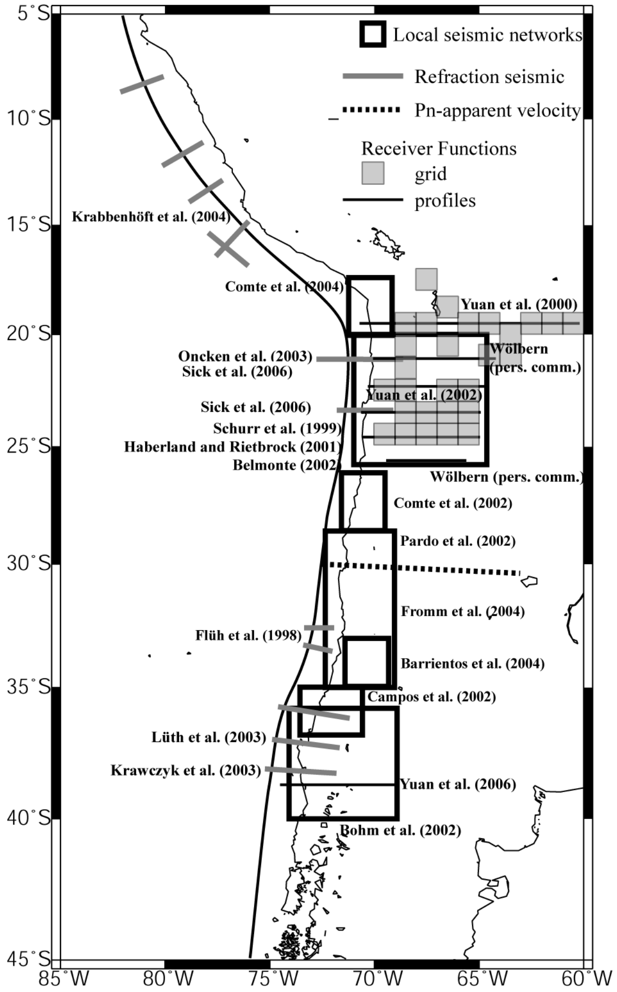

Figure 4

Figure 4. Distribution and references of locally generated seismic information incorporated into the 3-D density model to constraint the geometry of the subducted slab (local seismic networks and refraction seismic profiles) and continental Moho (Pn apparent velocity and receiver function results).

[29] The resulting slab geometry is best constrained in regions like the central Andes between 20° and 25°S where seismic profiles, receiver function observations and local

seismic networks are available and the global tomography model is well constrained. For these regions, we estimate an uncertainty in slab position of ±5 km at 150 km depth based on the standard average error for hypocenter locations [e.g., *Hacker et al.*, 2003b]. The slab geometry is poorly defined in other regions, like the southern Andes south of 40°S, where no local data are available, teleseismic information is intrinsically scarce at all depths, and the global tomography model is poorly resolved. In this region, uncertainties in slab position can be as high as ±25 km at 150 km depth.

5.3. Continental Lithosphere–Asthenosphere Boundary

[30] We shape the geometry of the continental LAB in our model mostly by fitting the intermediate- to long-wavelength Bouguer anomaly, but also by simultaneously maintaining consistency with two independent data sets: the heat flow map of South America of *Hamza and Muñoz* [1996] and continental-scale seismic tomography models of *Vdovin et al.* [1999], *van der Lee et al.* [2001] and *Feng et al.* [2004]. To do this, we accept that the LAB beneath the continent is thermally defined as the depth at which the conductive thermal gradient characteristic of the lithosphere intersects an asthenospheric adiabat [e.g., *Artemieva and Mooney*, 2001] and therefore that variations in LAB depth should be positively correlated with the intermediate- to long-wavelength distribution of surface heat flow density *Qs* (see Appendix A). In addition, and as pointed out by *Feng et al.* [2004], the subcrustal seismic velocity structure is primarily sensitive to mantle temperature variations and hence to the LAB depth. During the modeling, we attempted to represent in the final LAB geometry the most robust features suggested by both the regional- to continental-scale variations of *Qs* reported by *Hamza and Muñoz* [1996], as well as the distribution of S wave velocities below 100 km and Rayleigh surface waves at periods greater than 60 s shown in the maps of *Vdovin et al.* [1999], *van der Lee et al.* [2001] and *Feng et al.* [2004]. The average estimated error in the LAB geometry resulting after this modeling is 10 km.

5.4. Continental Moho

[31] The Moho discontinuity is fixed in the model based on the results of seismic experiments in some regions of the Andean margin (Figure 4). Most of these data have been produced in the framework of the SFB267 project. Receiver function analysis of locally recorded earthquakes along the central Andes between 20° and 25°S were published by *Yuan et al.* [2000, 2002]. Using two different methods, they observed a P-to-S seismic wave velocity converter at the base of the continental crust and reported depths to the Moho. As discussed in the original papers, these estimates are generally in good agreement with published data obtained from deep seismic refraction profiles [*Wigger et al.*, 1994; *Schmitz et al.*, 1999] and other receiver function studies [e.g., *Beck et al.*, 1996]. However, *Yuan et al.* [2002] do not discuss the reason why their estimates from a grid search algorithm are up to 10 km shallower than those reported by *Yuan et al.* [2000] based on stacking and depth migration of the receiver functions along EW profiles. We used a Moho depth in between these two estimates to represent the Moho geometry along profiles where both results are available.

[32] *Yuan et al.* [2006] also report a receiver function profile at 39°S, from which we have digitized the Moho depths obtained after correcting the depth-migrated receiver functions by the results of the grid search method. Two additional unpublished receiver function profiles imaging the continental Moho at 21°S and 25.5°S were provided by I. Wölbern (personal communication, 2004). *Fromm et al.* [2004] estimated Moho depths from an analysis of apparent Pn wave phase velocities recorded along an EW array of broadband seismic stations around 30°S. These estimates are in good agreement with those published by *Regnier et al.* [1994].

[33] For unconstrained regions, the Moho was shaped by fitting the intermediate-wavelength Bouguer anomaly along each modeled cross section, maintaining a smooth transition to seismically constrained regions and following the general trend of surface elevation under the assumption that the orogenic topography is primarily compensated by a crustal root. By doing this, we follow the main conclusions of previous isostatic analyses of the Andes [e.g., *Götze et al.*, 1991, 1994; *Introcaso et al.*, 1992; *Tassara and Yáñez*, 2003] and elsewhere [e.g., *Lowry et al.*, 2000; *Watts*, 2001], but note that we made no attempt to fix the Moho geometry from predictions of either Airy or flexural isostatic compensation models.

[34] On the basis of the previously mentioned discrepancy between different receiver function methods, the average thickness of converters at the base of the crust along receiver functions profiles and the sensitivity analysis of *Fromm et al.* [2004], we estimate the average uncertainty in Moho depth to be ±5 km in regions where it is seismically constrained.

5.5. Intracrustal Density Discontinuity

[35] The geometry of the ICD is not constrained by independent information. Instead, it is adjusted to remove any misfit to the observed Bouguer anomaly that remains at intermediate to short wavelengths after fixing the Moho and subcrustal density structure in the manner described above.

6. Residual Bouguer Anomaly and Model Accuracy

[36] The quality and accuracy of the model can be quantified by its ability to reproduce the observed gravity field. Figure 5 shows a residual Bouguer anomaly map computed by gridding the differences between observed and calculated Bouguer anomaly for each gravity station contained in the database. Less than 10% of the studied region has residual anomalies with amplitude greater than the estimated error in the observed Bouguer anomaly (±20 mGal). These anomalies are of very short to short wavelength and are not systematically distributed in the map.

[37] At wavelengths relevant to this work (i.e., greater than some hundred kilometres), the residual anomalies lie well within the range ±20 mGal. The histogram in Figure 5 shows a tight concentration of residual anomaly values around 0 mGal, defining a standard deviation of 15.05 mGal. These statistics indicate that the 3-D density model satisfactorily reproduces the regional- to continental-scale features of the observed Bouguer anomaly with an accuracy better than the error in the measured anomaly. This means

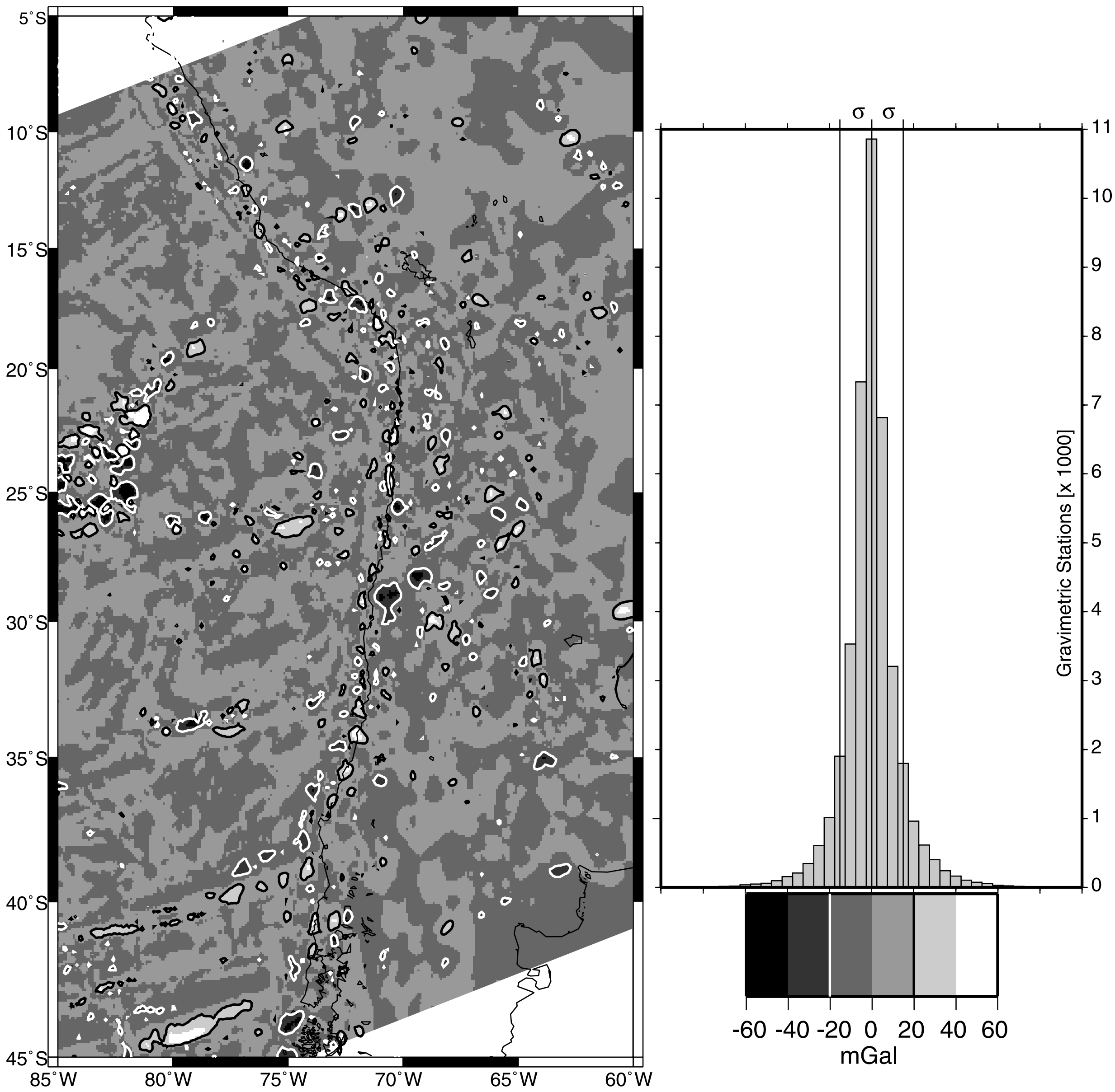

Figure 5. Residual Bouguer anomaly generated by the final model. The residuals were calculated for each gravimetric station as the difference between observed and calculated Bouguer anomaly. Regions delimited by white and black contours have anomalies lower than −20 mGal and higher than 20 mGal, respectively. More than 90% of the modeled area has residuals between these limits. The histogram shows a tight concentration of residuals around zero with a standard deviation σ = 15.05 mGal.

that the model is a good representation of mass distribution along the Andean margin.

7. Sensitivity Analysis

[38] We used a facility of IGMAS to test the sensitivity of the final model to changes in density and geometry. We estimated the uncertainty in the density selected for each body as the tolerable percentage variation in this parameter that would produce a variation in the calculated Bouguer anomaly equal to the estimated error of the observed anomaly, i.e., ±20 mGal. These uncertainties are presented in Table 2a. The average uncertainty resulting from changes in the depth to density discontinuities is shown in Table 2b. To estimate these uncertainties, for several cross sections of the model we calculated the vertical variation of the vertices defining each discontinuity that produce an average change in the calculated Bouguer anomaly equal to the tolerance limit of ±20 mGal. The uncertainty associated with each discontinuity should be less than that of the vertices. This is because the 3-D effect on the gravity field produced by vertically moving the whole discontinuity is larger than the effect of moving single vertices. We estimate the expected uncertainty in the depth of each discontinuity to be 20% of the average uncertainty calculated for single vertices.

[39] This analysis and the information summarized in Table 2a give an indication of the tolerable range of variation in densities for each body and the geometry of

Table 2a. Uncertainties of Allocated Density Values Resulting From the Sensitivity Analysis[a]

	Oceanic Plate and Subducted Slab										Continental Plate				Asthenosphere			
	m		a		b		c		d									
Segment	OC	OM	OC	OM	OC	OM	OC	OM	OC	OM	UC	LC	WM	EM	OA	LA	WA	EA
I	2.31	0.30	2.95	0.49	5.75	0.96	6.32	0.97	7.07	1.14	0.92	0.32	0.40	0.15	0.06	0.06	0.36	0.23
II	2.00	0.27	3.03	0.42	5.03	0.69	6.39	0.94	8.73	1.25								
III	1.40	0.21	2.78	0.45	3.78	0.50	4.57	0.58	7.63	0.94								
IV	1.37	0.18	3.83	0.51	4.34	0.44	5.48	0.58	7.23	0.77								
V	0.65	0.15	3.60	0.42	4.12	0.41	6.03	0.61	9.85	1.14								
VI	0.85	0.18	1.34	0.42	2.23	0.44	2.42	0.44	7.74	0.80								
VII	2.42	0.21	2.88	0.41	3.59	0.45	3.81	0.47	6.84	7.14								

[a] Abbreviations are as in Table 1. All values are absolute magnitudes. Uncertainties in density are tolerable percentage change with respect to the density values for the corresponding body in Table 1.

the discontinuities separating these bodies. This approach is by no means a tool to evaluate the accuracy of the model and it does not guarantee the resolution of the method. However, this information can be used to analyze the meaning of the final geometry obtained for density discontinuities that are not constrained by independent information. We discuss some specific aspects to be taken into account during the description and interpretation of the model.

[40] Densities of the oceanic mantle lithosphere could change by 0.15–0.3% with respect to the selected values without a noticeable change in the modeled Bouguer anomaly. Therefore and considering the calculations in Appendix A (Figure A2a), the model is sensitive to variations in the oceanic mantle density produced by a change in plate age of ±5 Myr. Such an age change for the Nazca plate does occur at scales of 500 km and its effect on the gravity field, namely the westward decrease of the Bouguer anomaly caused by decreasing average mantle density, is incorporated into the model by shifting the oceanic LAB downward by more than 8 km, i.e., by an amount equivalent to the uncertainty in the depth to this discontinuity.

[41] For continental mantle bodies, the calculated uncertainties in density between 0.15 and 0.4% and 10 km in the LAB depth, reflect a tolerable change in the surface heat flow of ±5 $\mathrm{mW/m^2}$ for cold foreland shield regions and up to ±10 $\mathrm{mW/m^2}$ for hotter orogenic regions (Figure A2b). Along some regions of the Andean margin, the surface heat flow changes at scales smaller than the size of mantle bodies (~200 km) and with amplitudes greater than the estimated tolerance limit (5–10 $\mathrm{mW/m^2}$ [*Hamza and Muñoz*, 1996]). These thermal anomalies with respect to the modeled mantle structure could produce a local misfit between observed and modeled Bouguer anomaly that will be compensated during the modeling by shifting unconstrained density discontinuities, i.e., the Moho in regions without seismic constraints and the ICD. The effect on the Moho could be of the order of ±5 km (Table 2b), which is identical to the uncertainty range associated with locating this discontinuity using seismic methods. This indicates that mantle density variations, at least those associated with regional fluctuations in the thermal field, will not cause major additional uncertainties in the Moho geometry. Similarly, compared with effects caused by lateral density variations within the crust, the effect of mantle density variations on the ICD geometry should be minor (~2 km, Table 2b).

[42] The selected density for the upper continental crust has an uncertainty of 0.92%. The empirical relationship between density and silica content for crystalline upper crustal rocks proposed by *Tassara* [2006] indicates that ~1% change in density around the selected value of 2.7 $\mathrm{Mg/m^3}$ is equivalent to a variation of ~5 wt % SiO_2 around the normal content of a granite (73 wt % SiO_2). For regions where the upper crust is mostly formed by crystalline rocks with a composition in this range, the geometry of the ICD will be dominated by the actual structure at the base of the upper crust and lateral density variations below this base. If the real upper crust locally comprises rocks with a density more than 1% lower or higher than 2.7 $\mathrm{Mg/m^3}$ (sedimentary basins or crystalline rocks with less than 68 wt % SiO_2), then the effect on the Bouguer anomaly will be higher than the tolerance limit of 20 mGal. This effect must be compensated in the model by vertically shifting the ICD by more than the 2 km estimated as the uncertainty for this discontinuity. In this way, the ICD geometry would also account for lateral density changes at upper crustal levels.

[43] A tolerable change of 0.32% for the lower crustal density indicates that the model is sensitive to density variations of up to 2.5% that can be produced by the extreme thermal differences between hot volcanic arcs and cold shields [*Tassara*, 2006]. The huge density uncertainties of ~15% related to the unknown lower crustal composition [*Tassara*, 2006] are even more important. In this context, the geometry of the ICD reflects the lateral variations in upper and mostly lower crustal composition, temperature within the lower crust and, to a minor extent, local thermal or compositional anomalies in the mantle.

8. Description and Discussion of Results

[44] We describe the main results of this modeling in terms of the final geometry of the density discontinuities that make up the 3-D model and discuss the implications of these results for some aspects of the geodynamics of the Andean margin. Tables S1–S6 list the vertices that define

Table 2b. Main Geometries[a]

Geometries	Value
Oceanic Plate	
Moho	1.5
LAB	8
Slab	
Upper surface	5
Continental Plate	
ICD	2
Moho	5
LAB	10

[a] Uncertainties in geometries are in km.

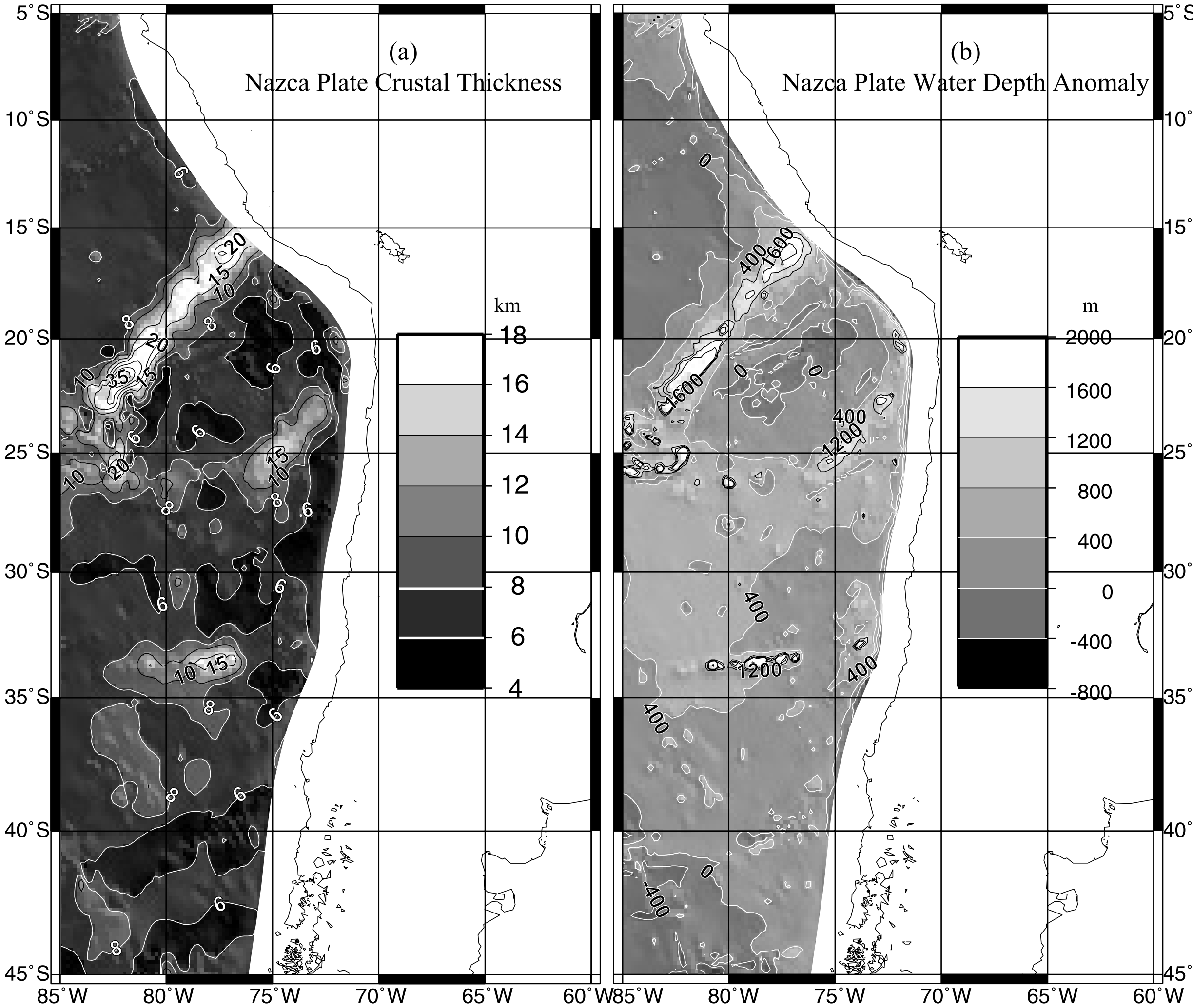

Figure 6. (a) Crustal thickness of the oceanic Nazca plate resulting from the model. Bold white contours are for isolines of 6 and 8 km, remarking the worldwide average oceanic crustal thickness of 7 ± 1 km [*Bown and White*, 1994]. (b) Water depth anomaly of the Nazca plate (see text for definition) for plate ages after *Müller et al.* [1997].

the geometry of each discontinuity in the final IGMAS model and are available in the auxiliary material[1].

8.1. Nazca Plate

8.1.1. Oceanic Moho

[45] The thickness of the oceanic crust obtained from the 3-D density model is shown in Figure 6a. This thickness has been calculated by subtracting the resulting oceanic Moho depth from the satellite-derived bathymetry. Only ~55% of the area covered by the Nazca plate in Figure 6a has a crustal thickness lying within the tight global range of 7 ± 1 km estimated by *White et al.* [1992] and *Bown and White* [1994]. This value reduces to ~45% if the more homogenous region to the north of the Nazca ridge is excluded.

[46] The anomalous distribution of crustal thickness correlates with the water depth anomaly (Figure 6b), i.e., the difference between observed bathymetry and water depths predicted by the half-space cooling model [*Turcotte and Schubert*, 2002, p. 175] for Nazca ages from *Müller et al.* [1997]. Regions with positive depth anomalies greater than 500 m are generally correlated with estimated crustal thickness greater than 8 km. This correlation suggests that these areas have been thermally uplifted after interaction with known hot spots (i.e., Easter, San Felix, Juan Fernández) and diffuse thermal anomalies (“Easter hot line” of *Bonatti et al.* [1977]), and injected with amounts of magma that exceed those generated along spreading centers. Depth anomalies greater than 1000 m along oceanic ridges are compensated by crustal roots in excess of 10 km thickness. The thickest oceanic crust is observed below the Nazca ridge, which shows a continuous crustal root with maximum crustal thickness of 35 km at the intersection of the ridge with the Nazca fracture zone. This is more than twice the maximum thickness of the Iquique and Juan Fernández ridges. The crustal root of the Juan Fernández ridge is discontinuous and does not thicken toward the trench. This is in agreement with the gravity-derived crustal thickness observed by *Yáñez et al.* [2002] and the refraction seismic tomography of *Kopp et al.* [2004].

---

[1] Auxiliary materials are available at ftp://ftp.agu.org/apend/jb/2005jb003976.

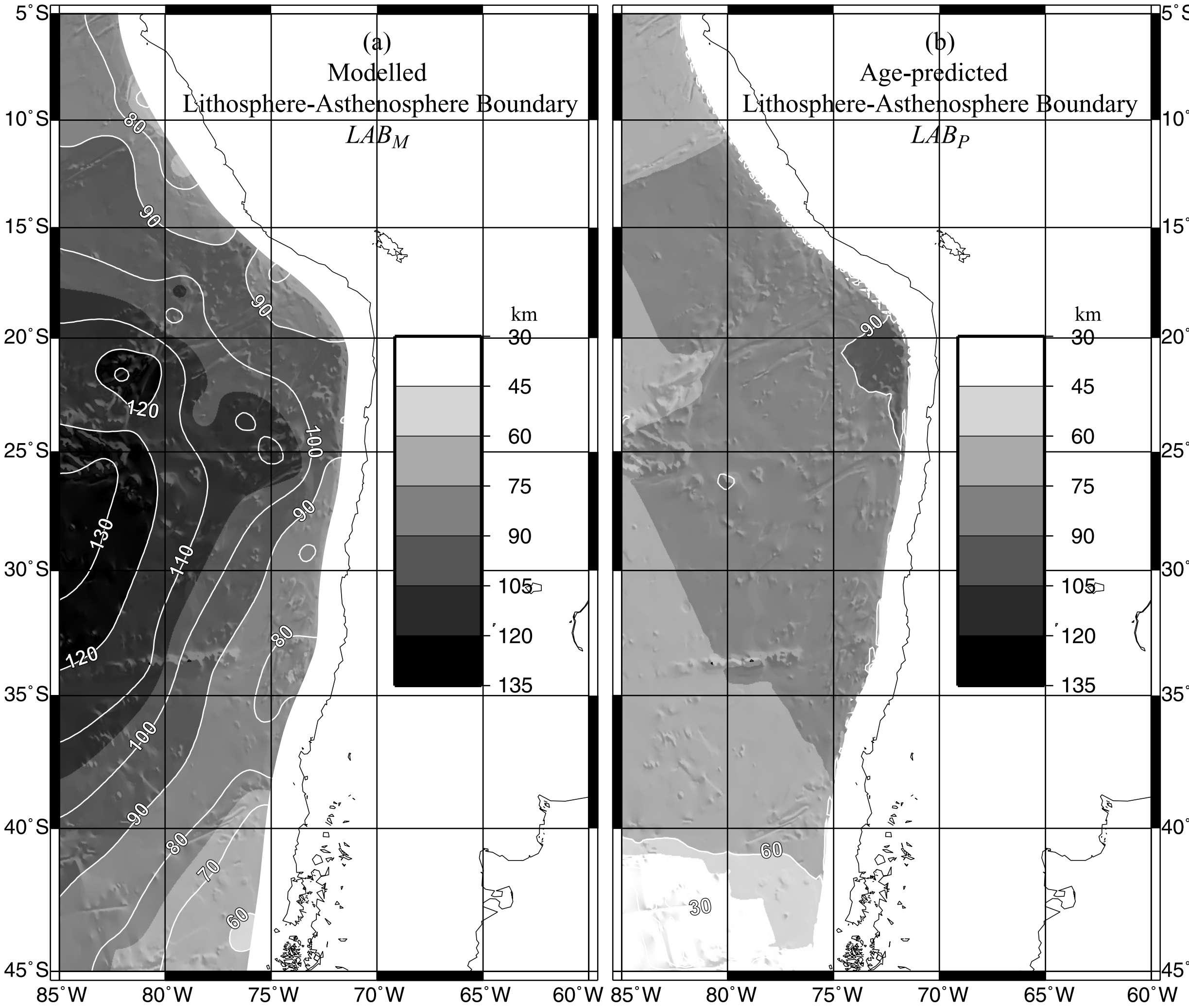

Figure 7. (a) Lithosphere-asthenosphere boundary (LAB) of the Nazca plate resulting from the model (LAB_M). (b) LAB depth predicted by an age-dependent half-space cooling model (see text) for Nazca ages after *Müller et al.* [1997].

[47] Neutral to negative water depth anomalies are correlated with thin oceanic crust (<6 km) along all fracture zones south of 15°S. Thinner crust along fracture zones is a common observation [e.g., *White et al.*, 1992]. The thick oceanic crust along the Chile Rise is not likely to be a real structural feature, but more an artefact of the model generated to compensate the presence of light molten material along the active ridge axis whose density should be much lower than the value selected for the crust of segments I and II.

8.1.2. Oceanic Lithosphere-Asthenosphere Boundary

[48] The depth to the oceanic LAB obtained from the density model (LAB_M) is shown in Figure 7a. Figure 7b shows the age-predicted LAB depth (LAB_P) calculated from a half-space cooling model as in Appendix A. LAB_P decreases and LAB_M increases west of the trench.

[49] The westward deepening of LAB_M represents the westward increasing mantle lithosphere mass deficit with respect to the density structure at the trench caused by the expected decrease in average density related to westward younging of the Nazca plate. In this context, the resulting LAB_M map of Figure 7a can be used to predict the oceanic mantle density structure expected under the thermal conditions implied by the half-space cooling model. In Appendix B, we explain a method to correct the densities of the oceanic mantle lithosphere considering the values selected for each segment (Table 1) and the maps of Figure 7 for modeled and age-predicted depths to the oceanic LAB. This correction essentially considers that the LAB depth must correspond to the prediction of the cooling model and then the spatial variations of LAB_M are converted to density variations with respect to the selected mantle lithosphere values by means of a simple mass balance. In Appendix B, we also show that the "corrected" density structure, after being included in the 3-D density model, reproduces the observed Bouguer anomaly, demonstrating the validity of such a correction. The corrected densities are shown in segments I to VII in Figure 8. The spatial variations obtained are now realistic, with a density decrease west of the trench and jumps across the fracture zones separating plate segments. However, unrealistically low density values were calculated for segments younger than 15 Myr, suggesting that the method described is not valid for extremely thin and hot lithospheres along the Chile Rise.

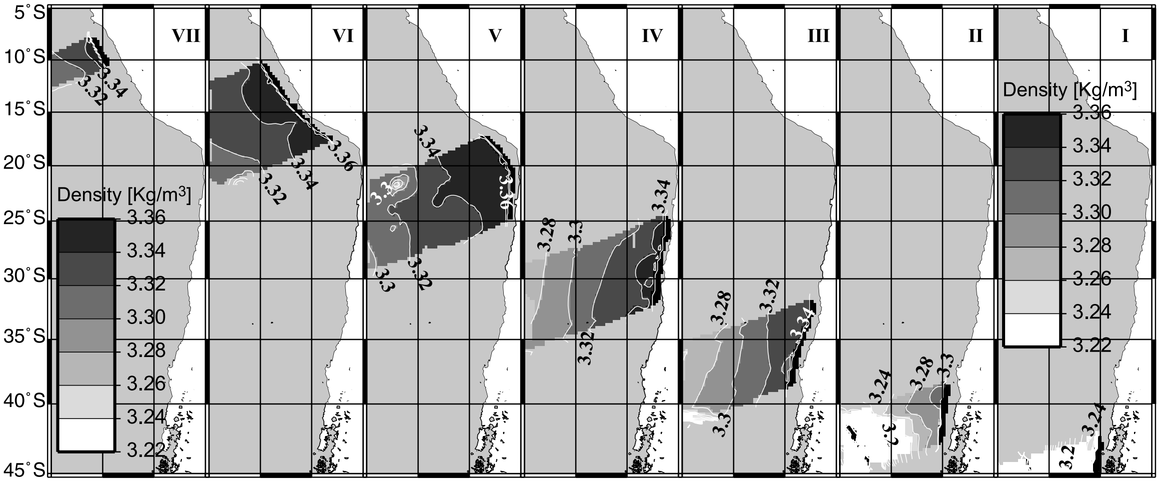

Figure 8. Corrected density structure of the Nazca plate lithospheric mantle. The results of the procedure discussed in the text and Appendix B for each of the seven modeled segments forming the oceanic plate are shown.

[50] At regional scales, reduced densities with respect to the surroundings can be observed along the Nazca ridge, particularly in its southwestern part (segment V). This correlates with the thickest oceanic crust estimated from the forward gravity modeling (Figure 6a). Both phenomena are related to the lowest Bouguer anomaly observed west of the trench region and suggest that, in addition to a thick crustal root, low lithospheric mantle densities also play a role in compensating the load of the Nazca ridge. This in turn could imply a thermally active lithospheric system that can be associated with the complex and poorly studied interaction of the ridge, the Nazca fracture zone and some deep thermal anomaly like that proposed by *Bonatti et al.* [1977]. Small-scale (<200 km diameter) zones of mantle density lower than the surroundings are also evident near the trench to the north of the Juan Fernández ridge (segment IV) and along the subduction region of the Mocha-Valdivia fracture zone (segment III). The low densities to the north of the Juan Fernández ridge are in good agreement with both the position and magnitude of reduced mantle seismic velocities inferred by *Kopp et al.* [2004]. They explained these low velocities by partial serpentinization of the uppermost mantle where an old hot spot-related fault system was reactivated once it reached the bent outer rise region. Enhanced mantle serpentinization could also explain low densities associated with the subducting Mocha–Valdivia fracture zone, for which the concentration of strike-slip deformation during its Neogene tectonic history [*Tebbens and Cande*, 1997] left a pervasively faulted uppermost mantle.

8.2. Subducted Slab

[51] The slab geometry obtained from the method described in section 5.2 is shown in Figure 9a. The inclusion of shaded topography, illuminated from the NE, allows a comparison with upper plate morphostructure. Continental-scale features of the subducting slab that are evident in Figure 9a are in good agreement with the slab geometry presented previously by *Cahill and Isacks* [1992], *Creager et al.* [1995], and *Gutscher* [2002]. In particular, coincidences are observed in the definition of (1) a relatively constant penetration angle (i.e., between the trench and 50 km depth) of ~20° between 5° and 36°S that decreases further to the south; (2) flat segments between 100 and 150 km depth associated with volcanic gaps in Peru (5°–15°S) and Argentina (27°–32°S); (3) steeply subducting segments with dip angles of 25–35° between flat slab regions; and (4) a general parallelism between trench axis, coastline, volcanic front and slab contours along the Arica Bend. Unlike previous models of slab geometry, the geometry shown in Figure 9a contains significant information at regional scales (hundred kilometres) because the database compiled for this model contains more information of better quality than was available for previous compilations.

[52] The slab geometry resulting from our model could be used for several tasks. In the following we only deal with the causes of slab flattening in the context of the relationship between the crustal structure of subducting oceanic ridges (Figure 6a), the position and morphology of flat slab segments and their remarkable correlation with the morphostructure of the continental plate (Figure 9a). These observations suggest that although the southern, shallow part of the Peruvian flat slab is obviously correlated with the subduction of the huge Nazca ridge, the positive buoyancy of subducted ridges with respect to the surrounding slab [e.g., *Gutscher et al.*, 2000; *Yáñez et al.*, 2001] is a necessary but insufficient condition for causing slab flattening. In particular, note that the subduction of the Iquique ridge, which has a more continuous crustal root than the Juan Fernández ridge in Figure 6a, is associated with a steeply subducting slab underneath the Altiplano region.

Figure 9. Geometry of density discontinuities underneath the continental margin that were constrained with independent data. Triangles are active volcanoes and the shading corresponds to topography-bathymetry. (a) Subducted slab contoured every 25 km. (b) Lithosphere-asthenosphere boundary (LAB) contoured every 20 km. (c) Moho every 10 km. In Figures 9b and 9c, dotted lines depict the intersection of the corresponding discontinuity with the subducted slab (white line) and the plane separating western and eastern mantle bodies (black line) (see also Figure 1b).

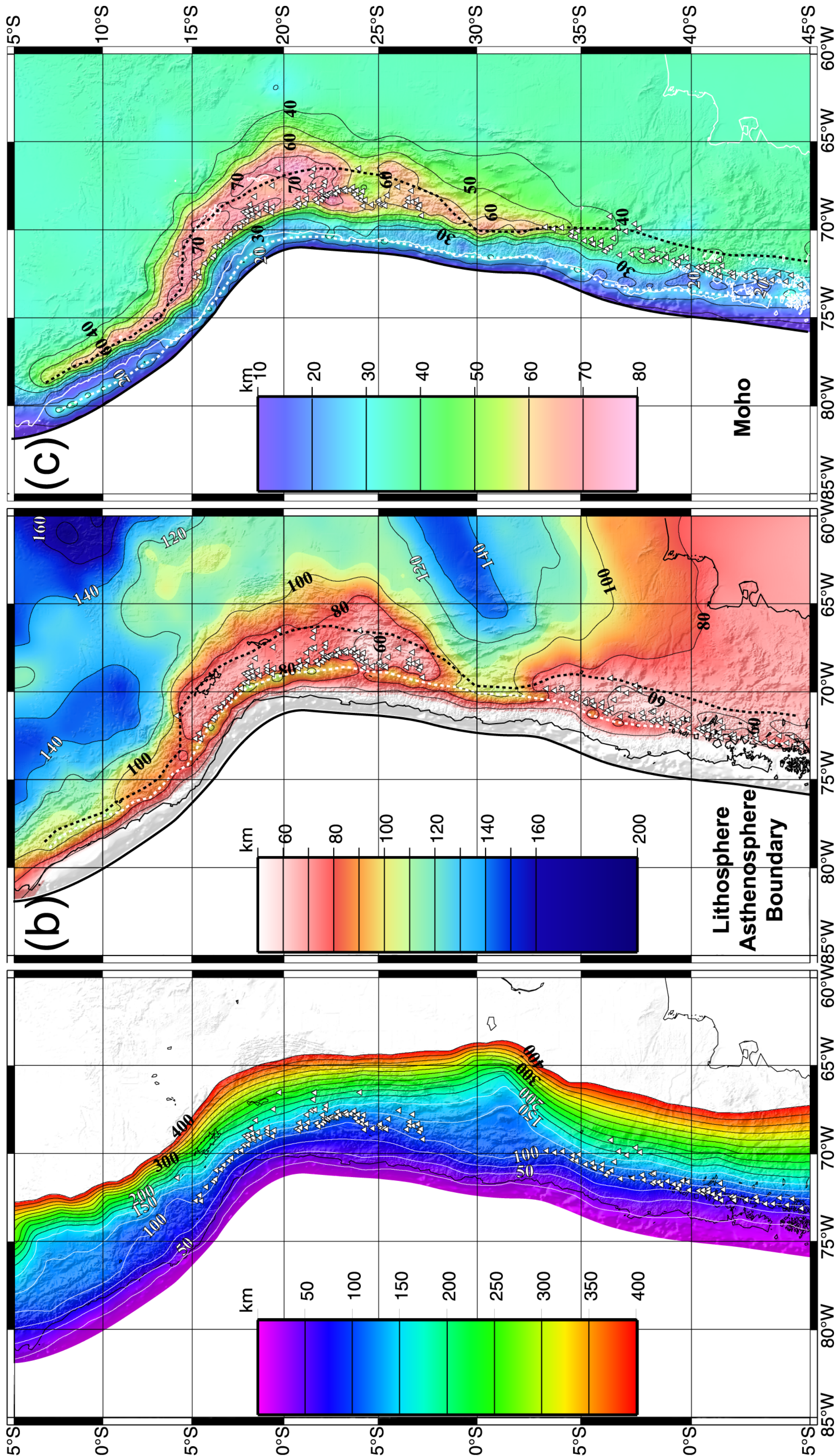
(b)
(c)
Lithosphere Asthenosphere Boundary
Moho
km
50
100
150
200
250
300
350
400
km
60
80
100
120
140
160
200
km
10
20
30
40
50
60
70
80
5°S
10°S
15°S
20°S
25°S
30°S
35°S
40°S
45°S
85°W
80°W
75°W
70°W
65°W
60°W

Figure 9

Two other factors to be considered as controls on the shape of the slab are (1) locally enhanced buoyancy of the oceanic plate caused by hydration of the uppermost mantle to the north of the Juan Fernández ridge, as revealed by seismic velocities [*Kopp et al.*, 2004] and density anomalies (Figure 8, segment IV), and (2) the dynamic control exerted by the absolute westward motion of the South American plate, as highlighted by the thermomechanical models of *van Hunen et al.* [2004]. This is also coupled to a decrease (from the Altiplano toward the Peruvian and Argentinean flat slab segments) in the amount of convergence that is absorbed by upper plate shortening [e.g., *Isacks*, 1988].

8.3. Continental Plate

8.3.1. Lithosphere-Asthenosphere Boundary

[53] The LAB depth below the Andean continental margin resulting from this modeling is shown in Figure 9b. We describe some continental-scale features of the LAB geometry that are robust with respect to the uncertainties derived from the gravity modeling and those related to the heat flow data [*Hamza and Muñoz*, 1996] and seismic tomography models [*Vdovin et al.*, 1999; *van der Lee et al.*, 2001; *Feng et al.*, 2004] used to constrain it.

[54] Active volcanic zones are underlain by lithosphere thinner than 80 km. This value reduces to 60 km below the central Puna and along the SVZ south of 36°S, where thinner crust (Figure 9c) allows the existence of shallower asthenosphere. As shown in Figures 9b and 9c, the mantle under volcanic zones is formed by the western bodies of Figure 2 that has a low density with respect to the eastern mantle bodies. This reflects their position underneath the hottest and most hydrated regions of the continental margin. The lithosphere below volcanic gaps and flat slab segments has the same properties as the cold and dense eastern body (EM in Figure 2 and Table 1) and is also thicker than 100 km.

[55] East of the main cordilleras, the LAB reaches depths greater than 120 km north of 12°S and along an ENE oriented region underneath the eastern Sierras Pampeanas. The northwestern limit of this region roughly correlates with the presumed suture between the Rio de la Plata Craton and the Pampean suspect terrain, and between the latter and the Cuyania terrain [e.g., *Ramos*, 1988; *Chernicoff and Zappettini*, 2003]. This suggests a first-order distinction between these lithospheric blocks. The thickest lithosphere within the study region (>160 km thick) underlies the eastern part of the Brazilian shield. This region is separated from the thick lithosphere underneath the Peruvian foreland (>140 km thick) by a NW oriented and relatively thin lithospheric corridor that connects with a wide zone of lithosphere thinner than 120 km underlying the western Brazilian shield and the foreland behind the Altiplano-Puna plateau.

[56] For regions not affected by arc volcanism, the thinnest lithosphere can be recognized east of the southern Andean cordilleras underneath the North Patagonian Massif, where LAB depths are less than 80 km. This region shows a gradual transition to the thick Pampean lithosphere to the north, which comprises NW oriented structures that can be recognized in the topography of the Neuquén System and San Rafael Block (see Figure 1a). This could suggest that the proposed Patagonian plate [e.g., *von Gosen*, 2003] is essentially different to the continental blocks to the north. The region of shallow LAB in Patagonia to the east of the Neuquén System and along the northern part of the North Patagonian Massif has been subjected to intense Cenozoic volcanic activity of presumed asthenospheric origin [e.g., *de Ignacio et al.*, 2001; *Kay et al.*, 2004]. This could be related to a persistent thermal anomaly that characterizes the Patagonian lithosphere.

8.3.2. Moho

[57] The depth to the continental Moho is shown in Figure 9c. We comment on some continental-scale characteristics of this geometry that, within the uncertainties previously discussed, can be considered first-order features of Andean crustal thickness.

[58] The modeled intersection of the continental Moho with the subducted slab along the central Andean forearc (white dashed line in Figure 9c) roughly coincides with the coastline, the 0 mGal contour line (Figure 1b), the 30–50 km depth range of the subducted slab (Figure 9a) and the downdip limit of the seismogenic zone (DLSZ) as defined by *Tichelaar and Ruff* [1991] and *Khazaradze and Klotz* [2003]. Thus the model suggests a strong causative relationship between these observables and also supports the main conclusion of *Oleskevich et al.* [1999] that the DLSZ corresponds to the intersection of the subduction thrust fault with serpentinized, nonseismogenic forearc mantle. Along the southern Andean forearc (mostly south of 38°S), the modeled Moho-slab intersection is shifted westward with respect to the DLSZ determined by *Khazaradze and Klotz* [2003]. This could indicate a seismogenic forearc mantle in this region, similar to that proposed for other subduction zones [e.g., *Simoes et al.*, 2004].

[59] East of the Moho-slab intersection, the crust is commonly thinner than 30 km and the Moho is upwardly convex. The forearc mantle is generally shallower than 20 km, particularly underneath the Peruvian coastline and the Central Valley south of 38°S. The thinned crust south of 38°S is consistent with seismic tomography results that image a shallow mantle below the southern Andean forearc [*Bohm*, 2003] and with Meso-Cenozoic extension of the forearc region [e.g., *Mpodozis and Ramos*, 1989].

[60] The high topography of the central Andean orogen is compensated by thick crust reaching more than 60 km thickness. This crustal root seems to be very narrow (<100 km) north of 13°S, widening southward as the Altiplano also widens. This part of the plateau is locally underlain by crust thicker than 70 km, with a maximum of ~75 km constrained by receiver function analyses (Figure 4) beneath the western limit of the Eastern Cordillera. In contrast to the thick Altiplano, the Puna shows a crustal root thinner than 55 km. Considering that the elevation here is almost 1000 m higher than in the Altiplano, *Isacks* [1988] and *Yuan et al.* [2002] proposed that the Puna is partially compensated by hot shallow asthenosphere, which can be observed in the resulting LAB map (Figure 9b). These features are consistent with the Late Neogene delamination suggested by some authors [e.g., *Kay and Kay*, 1993; *Allmendinger et al.*, 1997] and restricts the occurrence of significant lower crustal removal to a region located in the central part of the Puna.

[61] South of 26°S, the high cordilleras are again underlain by a Moho deeper than 60 km. The morphology of the crustal root along the southern central Andes seems to be affected by the complex structural interaction between the

Frontal Cordillera, the Argentinean Precordillera and western Sierras Pampeanas (Figure 1a), further suggesting the presence of lithospheric-scale discontinuities between different continental terrains. Along the Principal Cordillera, the crustal thickness gradually decreases from 60 to 40 km. Around 36°S, we observe a local minimum of the crustal thickness that can be connected to a NW oriented region of thin crust (<35 km) to the east. This region was constrained by receiver function results at 39°S and is correlated with upper crustal structures recognizable in topography and associated with active back-arc volcanism [e.g., *Folguera et al.*, 2002; *Kay et al.*, 2004]. The central segment of the SVZ (37°–40°S) overlies crust ~40 km thick, but this value seems to decrease to less than 30 km along the southernmost SVZ. In this region there are no seismic constraints and the shallow Moho could be indicating the presence of dense mantle and/or crustal material.

8.3.3. Intracrustal Density Discontinuity

[62] The depth to the ICD is shown in Figure 10a. This is a result of our model that is independent of other geoscientific information, and therefore it can be used to gain new insights into the three-dimensional mass distribution within the Andean continental crust. Owing to the multiple factors potentially affecting the ICD geometry, its interpretation is a complex task that should be undertaken with the assistance of independent information.

[63] In an attempt to evaluate the effect of upper crustal density variations, we produced a map showing the percentage difference between surface density and the value of 2.7 Mg/m^3 selected for the upper crust. This map was generated using the digital geological map of South America [*Schobbenhaus and Bellizzia*, 2001], which describes first-order geological units. Applying standard density values [e.g., *Carmichael*, 1989; *Tassara*, 2006] for the lithologies described in this map and then calculating for each geological unit the percentage difference with respect to 2.7 Mg/m^3, we ended up with the map of Figure 10b. We note that this map is useful for assisting the interpretation of the ICD geometry, as shown below, but a deeper and more robust interpretation for specific regions should consider a more detailed surface density map and seismic velocity models against which the internal structure suggested by the ICD can be tested.

[64] We advance a general interpretation of some interesting features evident in Figure 10. We note an anticorrelation between the depth to the ICD and surface density. In regions where high-density rocks are exposed at the surface, the ICD is shifted upward by an amount that should depend on the volume of these units. For instance, Cenozoic basaltic lavas covering the eastern Neuquén System and North Patagonian Massif (5–8% higher than 2.7 Mg/m^3 in Figure 10b), coincide with regions where the ICD is deeper than 10 km. This suggests that they are thin sheets overlying a basement likely dominated by felsic Late Paleozoic rocks [e.g., *Mpodozis and Ramos*, 1989]. In contrast, Meso-Cenozoic intermediate-to-basic igneous rocks outcropping along the central Andean Coastal Cordillera and the Patagonian Cordillera and characterized by densities some percent higher than the selected value of 2.7 Mg/m^3, are consistently associated with an ICD shallower than 5 km. The spatial continuity of this shallow ICD zone indicates that such high-density rocks likely form the entire crust along the central Andean forearc (including its offshore region) and that they could be connected with the Patagonian Batholith below the Cenozoic cover of the northernmost southern Andes. Similarly, the Early Palaeozoic high-density mafic-to-ultramafic rocks outcropping along some of the western Sierras Pampeanas seem to be the surface expression of a larger terrain characterized by ICD depths shallower than 7.5 km and presumably by high crustal densities. The extent of this region in Figure 10a coincides with the presumed location of the suspected Cuyania terrain [*Ramos*, 1988; *Chernicoff and Zappettini*, 2003], supporting its characterization as a mafic-dominated block that is probably allocthonous with respect to the dominantly felsic Andean basement [e.g., *Lucassen et al.*, 2004]. However, the ENE oriented nature of regions where the ICD is shallower than 5 km and their correlation with seismic velocity anomalies at mantle depths, as imaged by *Wagner et al.* [2005], suggest that this ICD feature could be partially associated with strong lateral density variations in the upper mantle that are probably produced by the subduction of the Juan Fernández ridge. As for other features observed in the ICD map, evaluating the real causes behind the observed patterns requires an integrated interpretation that includes crustal seismic velocity models.

[65] Figure 10b also shows that most of the rocks outcropping along the central Andean orogen have a density differing from the modeled upper crustal value by a magnitude similar to the tolerable uncertainty for this body, i.e., ±1%. For this region, the ICD geometry should reflect the structural discontinuity between upper and lower crust and variations of lower crustal density with respect to the value selected for the model. In this context, one of the strongest features observed in Figure 10a is an ICD generally deeper than 15 km between 7° and 29°S underneath the axis of the central Andean orogen, reaching values greater than 25 km to the north and south of the Altiplano. This deep ICD suggests a large felsic component in the orogenic crust, at least larger than beneath the cordilleras south of 36°S, where an ICD shallower than 10 km suggests a mafic-dominated crust. Note that heat flow data [*Hamza and Muñoz*, 1996] and the LAB geometry of Figure 9b suggest a similar thermal state along the central Andean plateau and the southern Andes that is likely characterized by high temperatures at lower crustal depths. This precludes a possible thermal effect on the observed difference in the ICD geometry for these regions and suggests that compositional differences are the main cause of the continental-scale Andean segmentation.

[66] Variations in ICD geometry along the central Andean plateau correlates with changing foreland deformation mechanisms. A shallower ICD along the central Altiplano (10–15 km) coincides with the flat detachment of the thin-skinned Sierras Subandinas, whereas toward the boundaries of the plateau, a deeper ICD (>15 km) correlates with thick-skinned deformation [*Isacks*, 1988; *Allmendinger and Gubbels*, 1996; *Kley et al.*, 1999]. This suggests that the crustal compositional structure exerts an important control on the deformation of the continental margin.

[67] An ICD no deeper than 25–30 km along the Altiplano-Puna plateau suggests that the bulk crustal composition is at most intermediate, but certainly not felsic, as suggested by some authors based on low P wave velocities (Vp ~6 km/s) at

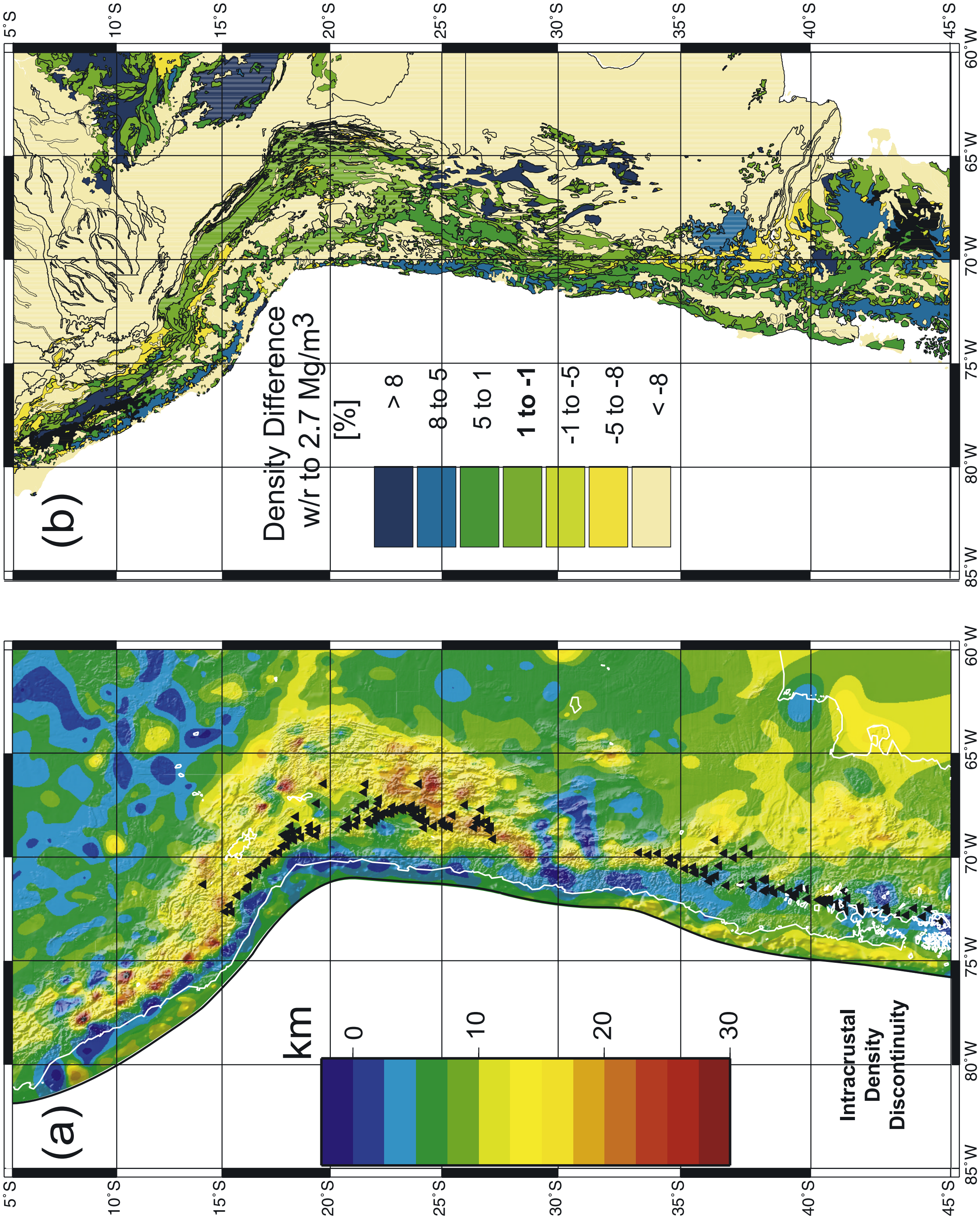
(a)
km
0
10
20
30
Intracrustal
Density
Discontinuity
(b)
Density Difference
w/r to 2.7 Mg/m^3
[%]
> 8
8 to 5
5 to 1
1 to -1
-1 to -5
-5 to -8
< -8
5°S
10°S
15°S
20°S
25°S
30°S
35°S
40°S
45°S
85°W
80°W
75°W
70°W
65°W
60°W

Figure 10

middle lower crustal depths [e.g., *Beck and Zandt*, 2002; *Yuan et al.*, 2002]. As proposed by *Schmitz et al.* [1997], the combination of low Vp and high density at lower crustal depths can be reconciled by substantial degrees of partial melting of a mafic protolith. The coincidence of high seismic attenuation (Qp = 100) and an extremely high electrical conductivity (1 S/m) down to 20 km depth below the Altiplano [e.g., *Haberland et al.*, 2003, and references therein] has been interpreted as a distinctive signal of high degrees of partial melting in the middle lower crust. This could also explain the low rigidity underneath the Altiplano [*Tassara and Yáñez*, 2003; *Tassara*, 2005] and low bulk viscosities ($10^{19}-10^{22}$ Pa s) required to produce the crustal flow thought to be partially responsible for the deformation pattern along the plateau [*Lamb*, 2001; *Yang et al.*, 2003; *Husson and Sempere*, 2003; *Hindle et al.*, 2005; *Gerbault et al.*, 2005]. We believe that our three-dimensional model could be combined in the future with available seismic velocity models in order to estimate the amount and distribution of partial melting present in the Altiplano and Puna crust, and to validate the compositional characterization proposed here for the plateau crust.

8.4. Reducing the Lower Crustal Density

[68] The density of 3.1 Mg/m^3 selected for the lower crustal body of the model is high compared with the range of values normally assumed by gravity modelers and implies that the density contrast across the ICD (0.4 Mg/m^3) is larger than across the continental Moho (0.22 Mg/m^3). This situation was criticized during the review of this paper, meaning that it is necessary to justify the use of the relatively high lower crustal density and to test the effect of reducing this density in the model.

[69] We prefer this high value mainly on the basis of the petrophysical analysis performed by *Tassara* [2006] to specifically provide an analytical tool to support the design of the model. This analysis demonstrated that a lower crustal density of 3.1 Mg/m^3 suitably represents the density of metaigneous rocks of andesitic to basaltic composition (60–50 wt % SiO_2) formed under middle to lower crustal pressure-temperature conditions (20–70 km depth) and over a wide range of water contents (dry to H_2O-saturated). Our choice of density allows the model to clearly differentiate a felsic upper crust (~70 wt % SiO_2) from intermediate-to-mafic lower crust and to map the lateral density variations inside the crust using changes in the ICD depth with respect to the reference model as a proxy for these variations. Recent gravity models presented by *Kozlovskaya et al.* [2004] and *Ebbing et al.* [2005] that are based in seismic velocity models, have lower crustal densities even higher than 3.1 Mg/m^3. In addition, some P wave tomography results reported for the Andean margin to the south of the Altiplano-Puna plateau, show velocities higher than 7.2 km/s at middle-to-lower crustal levels [e.g., *Pardo et al.*, 2003; *Bohm*, 2004], which according to the petrophysical modeling of *Sobolev and Babeyko* [1994], imply a mafic lower crustal composition with densities greater than 3.1 Mg/m^3. A density contrast at middle crustal levels that is greater than the contrast across the Moho in our model is also supported by seismic tomography models that show a smooth velocity gradient across the Moho [*Pardo et al.*, 2003; *Bohm*, 2004] and receiver function studies for the central Andes that commonly image an upper-to-middle crust P-to-S wave converter that is more intense than the one marking the continental Moho [*Yuan et al.*, 2000; *Beck and Zandt*, 2002].

[70] These arguments build a foundation for the high density value selected for the lower crust in the model. Nevertheless, we have evaluated the effects that a reduction in the lower crustal density would have on the final 3-D model. We reduced the density of the lower crust from 3.1 to 3.0 Mg/m^3, both in the reference model and in the 3-D structure. The density and geometry of other bodies remained the same. In this case, the average crustal density of the reference model is ~2.88 Mg/m^3 (i.e., similar to the average density traditionally assumed for the continental crust [e.g., *Christensen and Mooney*, 1995; *Turcotte and Schubert*, 2002]) and the Moho is the largest density contrast below the continent. Rather than readjusting the entire model, we calculated the residual Bouguer anomaly produced by this different configuration. The map and histogram of Figure 11, which were generated in the same way as Figure 5, help to identify the changes in densities and/or geometries of the original model that are necessary in order to reachieve the fit between observed and calculated Bouguer anomaly. For instance, we observe a systematic shift of -100 ± 20 mGal between both anomalies for the oceanic region. This shift is produced by the increase in the positive density contrast between the lithospheric mantle of the 3-D model and the lighter lower crust of the new reference model. This shift is 5 times greater than the error in the observed Bouguer anomaly. Considering Tables 2a and 2b and preserving the original oceanic Moho and LAB geometries, the misfit has to be compensated by decreasing the densities of oceanic crust or lithospheric mantle by ~5% and 1%, respectively. Considering the high density values required for the original model (Table 1) to fit the Bouguer anomaly at the trench, this reduction could have some justification. Whatever the case, this would be a systematic change that would not affect the main conclusions reached in section 8.1 with respect to the relative spatial variations in oceanic crustal thickness and mantle density structure.

[71] Most of the forearc and foreland regions and the entire continent south of 36°S show residual Bouguer anomalies in the range ±20 mGal (Figure 11). This implies that for these areas, reducing the lower crustal density has an effect on the calculated gravity field that cannot be resolved by the available data and hence no changes in the original 3-D model are necessary. This is not the case for the central Andean orogen. In this region, the thick crustal root and larger density contrast across the Moho generate a significant mass deficit and a shift of 40 to 120 mGal between observed and calculated Bouguer anomaly. Assuming that the subcrustal density structure is relatively well-constrained in this region, this positive shift must be compensated either by moving the ICD upward by several

Figure 10. (a) Geometry of the intracrustal density discontinuity (ICD). Triangles are active volcanoes and the shading corresponds to topography-bathymetry. Contours every 5 km. (b) Map representing the percentage difference between density of geological bodies at the surface and the density value selected for the modeled upper crustal body (see text).

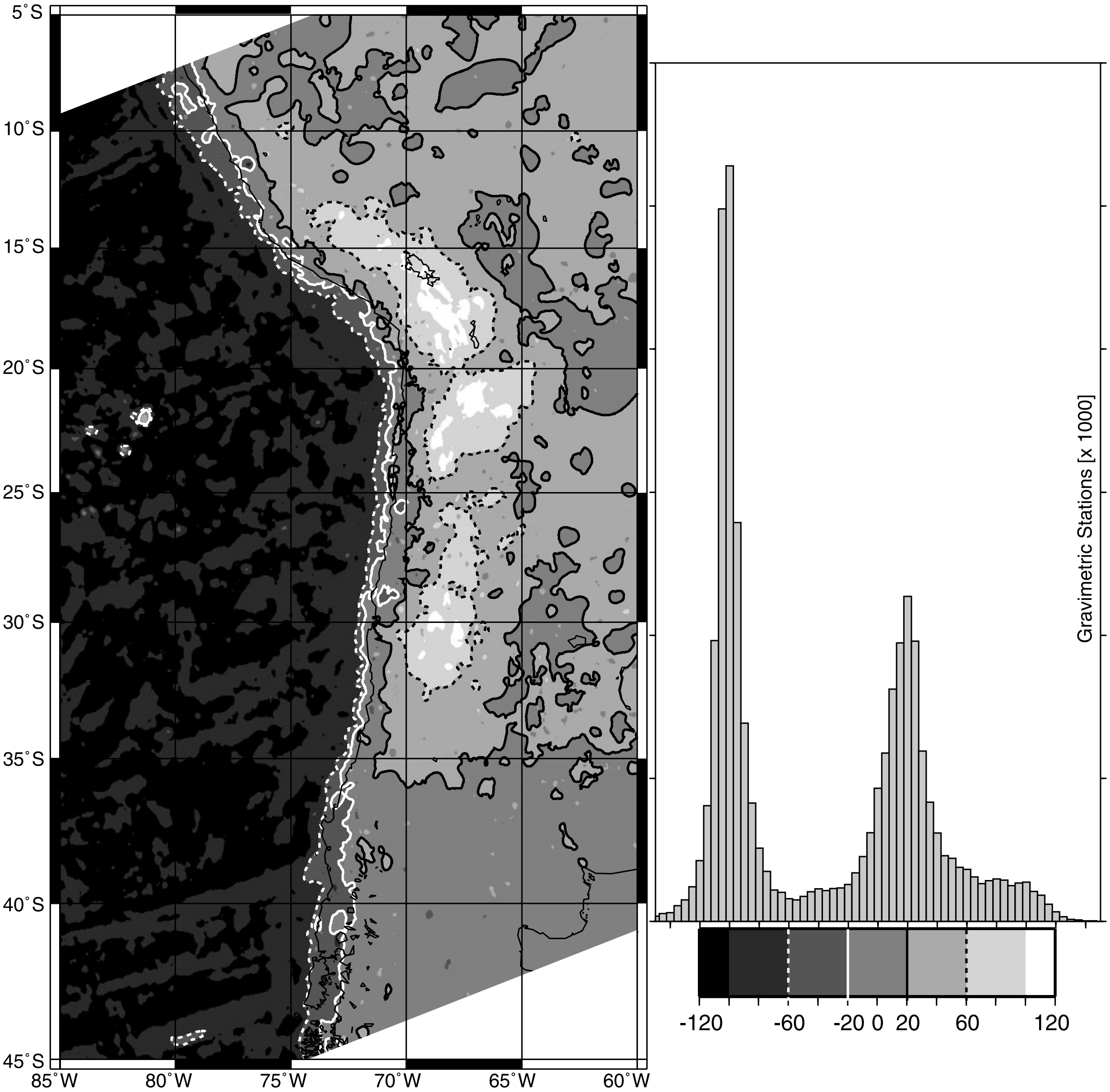

Figure 11. Residual Bouguer anomaly map and histogram as calculated for Figure 4, but after reducing the density of the lower crustal body of the 3-D model and the reference model from 3.1 to 3 Mg/m^3. White contours are for −20 mGal (bold) and −60 mGal (dotted); black contours are for 20 mGal (bold) and 60 mGal (dotted).

kilometres or by increasing the densities of mantle bodies and/or the slab. According to the information summarized in Tables 2a and 2b and considering the large volume of the asthenospheric mantle body below the plateau (WA, Figure 2), the misfit could be avoided by increasing the density of this body by at least 1%. However, based on the thermal analysis in Appendix A and the fact that this body is positioned under the hot and hydrated mantle wedge, a 1% increase in density is unrealistic. The other possibility is to increase the density of the slab bodies *c* and *d* (Figure 2) by 3–5%. Although the poor knowledge of the density structure of the subducted slab allows such a density increase, it would be necessary to explain why this increase occurs only below the central Andes. We conclude that reducing the lower crustal density from 3.1 to 3.0 Mg/m^3, would be best compensated by shallowing the ICD and hence increasing the proportion of intermediate-mafic material that forms the crust. In this case, the main compositional characterization of the Andean crust inferred from the ICD geometry of the original model is unchanged. We think that a systematic comparison of the ICD geometry derived from the model with existing seismic velocity models and geochemical parameters could help in the future to quantitatively constrain these scenarios and to gain better insight into the compositional structure of the Andean crust.

9. Summary and Conclusions

[72] We have presented a 3-D density model covering the Nazca plate (85°W) and the Andean continental margin

(60°W) between northern Peru (5°S) and Patagonia (45°S) that incorporates a simplified representation of density structure to 410 km depth. This inferred density structure is the result of forward modeling of the Bouguer anomaly with constraints from a compilation of independent (mostly seismic) data to fix the geometry of the subducted slab, locally the Moho of the oceanic and continental crusts, and indirectly the lithosphere-asthenosphere boundary (LAB) underneath the continental plate. The allocation of densities for the bodies forming the model is supported by a quantitative analysis that considers density to be a function of the chemical and mineralogical composition of rocks and pressure-temperature conditions appropriate for the Andean setting. A sensitivity analysis allows the uncertainties associated with the modeling to be quantified and provides a tool for interpreting the meaning of unconstrained density discontinuities.

[73] After describing and discussing the geometries of the major density discontinuities of the model, significant conclusions can be drawn that are related to the geodynamics of the Andean margin. For instance, the coincidence between water depth anomalies and the heterogeneous spatial distribution of crustal thickness for the oceanic Nazca plate compared with the worldwide average of 7 ± 1 km [e.g., *White et al.*, 1992], suggests that it has been substantially modified by the interaction with hot spots and diffuse thermal anomalies since its creation. These interactions resulted in some modification of the mantle density structure, which seems to also be affected by enhanced hydration near fracture zones and the trench. The southern Peruvian and Argentinean flat slab segments are associated with the prolongation of the Nazca and Juan Fernández ridges, respectively, but the Iquique ridge, which has dimensions similar to the Juan Fernández ridge, does not generate a flat slab below the Altiplano region. This suggests that the subduction of oceanic ridges is a necessary but insufficient condition for the flattening of the slab, an interpretation that is in agreement with conclusions drawn from numerical modeling [e.g., *van Hunen et al.*, 2004].

[74] Below the continental margin, our model shows interesting variations in the LAB depth that can be correlated with thermomagmatic segmentation (LAB < 80 km depth along the active volcanic zones; LAB > 100 km depth along volcanic gaps associated with flat slab subduction) and the pre-Cenozoic configuration of the margin (LAB > 120 km depth below Rio de la Plata Craton and suspected Pampia terrain; LAB > 160 km depth below the eastern Brazilian shield). The Patagonian terrain (or plate [*von Gosen*, 2003]) in the southeastern part of the study region shows extremely thin lithosphere (LAB < 80 km depth) for its position eastward of the main volcanic arc. This could be associated with the thermal anomaly that produced the Cenozoic alkaline volcanism characteristic of Patagonia.

[75] Variations in the morphology and thickness of crustal roots underneath the high Andean cordilleras (~75 km below the Altiplano region; <40 km along the southern Andes) and their spatial relation with surface topography and amounts of crustal shortening, suggest large- and small-scale variations in the isostatic mechanisms compensating the mountain chain and the processes that lead to construction of the Andean orogen. As inferred by previous authors, the main compensation mechanism seems to be related to thick and buoyant crustal roots [e.g., *Götze et al.*, 1991; *Introcaso et al.*, 1992; *Tassara and Yáñez*, 2003], but mantle thermal roots, elastic flexure, lateral density variations, and dynamic support from mantle and lower crustal flow could be also acting to partially compensate the cordilleran topography. Understanding the interaction between these processes can be supported by the Moho geometry of our 3-D model, but this task should also consider the internal crustal structure that can be inferred from the intracrustal density discontinuity (ICD) separating light upper crust from dense lower crust in the model. The ICD is a proxy for the lateral density variations produced mostly by changes in crustal composition, but also in lower crustal temperature and possibly the degree of hydration and partial melting of crustal rocks. Separating these effects requires the consideration of independent data such as the surface density map presented in this work or seismic velocity models for specific regions. When efficiently combined with such data, the ICD geometry can provide useful information on the mass distribution within the continental crust. Into this context, one important conclusion suggested by the ICD geometry is that the long-term, continental-scale Andean segmentation is likely caused by difference in the crustal composition from intermediate-to-felsic along the central Andes to mafic for the southern Andes.

[76] We believe that the 3-D density model presented here is a valuable contribution to the Andean geoscientific community. The 3-D structure is the final result of our modeling efforts, but we consider the modeling to be a starting point for moving toward an integrated understanding of Andean geodynamic processes. Auxiliary material Tables S1–S6 contain the vertices that define the geometry of major density discontinuities.

Appendix A: Mantle Density Structure

[77] To examine the density structure of the mantle, we use the Excel Macro released by *Hacker and Abers* [2004]. This tool implements the work of *Hacker et al.* [2003a] to calculate several physical properties (including density) of a predefined mineral assemblage at a given pressure-temperature (PT) condition. This tool was modified to read physical conditions from an one-dimensional PT gradient in order to calculate density profiles downward the lithosphere. Pressures are defined by a lithostatic gradient:

$$P(z) = \rho g z \tag{A1}$$

where z is depth, $\rho = 3$ Mg/m^3 is an average density and $g = 9.8$ m/s^2 is acceleration of gravity. Lithospheric temperatures are calculated along conductive geotherms. For the oceanic plate the geotherm follows a half-space cooling model [*Turcotte and Schubert*, 2002, p.161]:

$$T_{OC}(z) = \Delta T\left[\frac{z}{z_{L0}} + \frac{2}{\pi}\exp\left(-\frac{\kappa\tau\pi^2}{z_{L0}^2}\right)\sin\left(\frac{z\pi}{z_{L0}}\right)\right] \tag{A2}$$

where $\Delta T = 1300$°C is the temperature difference between top and bottom of the oceanic lithosphere, $z_{L0} = 2.32(\kappa\tau)^{0.5}$ is the thermal thickness of the plate, $\kappa = 1$ mm^2/s is the thermal diffusivity and τ is the age of the oceanic plate. The continental thermal structure is defined by a conductive

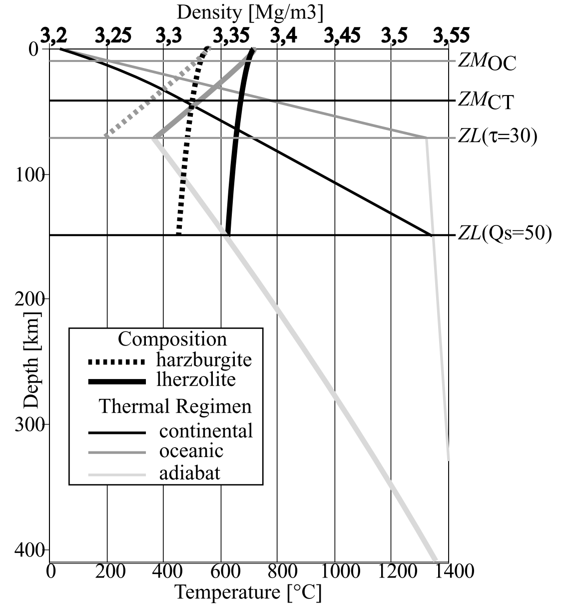

Figure A1. Density profiles (thick lines) calculated as explained in the text for harzburgite (dotted line) and lherzolite (bold line), and temperature gradients (thin lines) for three thermal regimes: continental (black), oceanic (grey), and adiabatic (light grey). This color code also holds for the density profiles. ZM is depth to the Moho (OC, oceanic; CT, continental) and ZL depth to the lithosphere-asthenosphere boundary ("τ = 30" means oceanic plate age of 30 Myr; "Qs = 50" means continental surface heat flow of 50 mW/m^2).

geotherm with crustal heat production decaying exponentially with depth [*Turcotte and Schubert*, 2002, p.147]:

$$T_{CT}(z) = Ts + \frac{Qs - \rho Hl}{k} z + \frac{\rho Hl^2}{k}\left(1 - e^{-z/l}\right) \qquad \text{(A3)}$$

Ts = 25°C is the surface temperature, H = 1 μW/m^3 is the crustal heat productivity, l = 10 km is the length scale for the decrease of H with depth, k = 2.5 W/m°C is the thermal conductivity and Qs is surface heat flow density. This parameterization defines the one-dimensional thermal structure of the oceanic lithosphere $T_{OC}(z)$ by the age of the oceanic plate τ, and that of the continental lithosphere $T_{CT}(z)$ by the surface heat flow density Qs. Examples of these geotherms are shown in Figure A1 for an oceanic plate age of 30 Myr and a continental heat flow of 50 mW/m^2.

[78] The asthenospheric thermal regimen is defined by an adiabat described by

$$T_A(z) = T_0 + Gz \qquad \text{(A4)}$$

where T_0 = 1300°C is the potential temperature reached at the Earth surface and G = 0.3°C/km is the adiabatic gradient.

[79] Figure A1 also shows density profiles calculated by coupling equations (A1) to (A4) with the macro of *Hacker and Abers* [2004] for two mineral assemblages; a spinel harzburgite ("hzG" in *Hacker and Abers* [2004]) and a garnet lherzolite ("pyrolite" of *Hacker and Abers* [2004]). These rocks represent mantle peridotites characterizing depleted continental lithosphere and fertile asthenosphere, respectively. The oceanic lithosphere, which is the residue left after much less amounts of basalt extraction than that producing the continental lithosphere [e.g., *Lee et al.*, 2005], would have an intermediate mineralogical composition between these end-members. From these density profiles we calculate an average lithospheric mantle density:

$$\overline{\rho} = \frac{1}{\mathrm{ZL} - \mathrm{ZM}} \int_{\mathrm{ZL}}^{\mathrm{ZM}} \rho(z)dz \qquad \text{(A5)}$$

with $\rho(z)$ being the variation of density with depth resulting from the computations and ZM and ZL the depth to the Moho and to the lithosphere-asthenosphere boundary (LAB), respectively. The latter is defined as the intersection of the conductive lithosphere gradient with the asthenospheric adiabat. Applying this procedure for oceanic plate ages between 5 and 50 Myr, continental surface heat fluxes between 45 and 85 mW/m^2 and ZM = 10 km for the ocean and ZM = 40 km for the continent, we compute variations of the average lithospheric density $\overline{\rho}$ for both selected peridotites as a function of τ and Qs. This is presented in Figure A2 that also shows the variations of ZL and the average densities of a pyrolite along the adiabat representing the asthenosphere. The latter was calculated with an expression similar to (A5), but integrating between ZL = 75 km (= LAB depth for a 30 Myr old oceanic lithosphere)

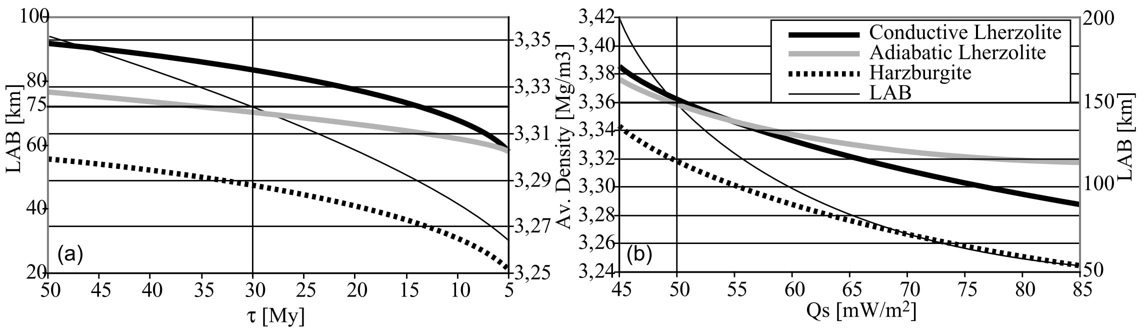

Figure A2. Average density (thick lines) of the mantle and depth to the lithosphere-asthenosphere boundary (thin line) calculated as explained in the text for two mantle peridotites as a function of (a) oceanic plate age and (b) continental surface heat flow.

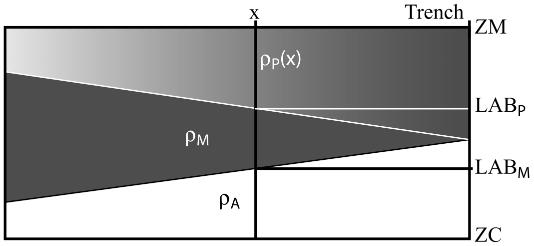

Figure B1. Schematic representation of the relationship between the lithospheric mantle structure of modeled oceanic plate and that expected for the half-space cooling model. The parameters are *x,* distance from the trench axis; ρM, density of the modeled lithospheric mantle body; ρA = density of the modeled asthenospheric mantle body; ZM, depth to the oceanic Moho; LAB_P, depth to the lithosphere-asthenosphere boundary predicted by the half-space cooling model; LAB_M, depth to the lithosphere-asthenosphere boundary from the model; ZC, an arbitrary compensation depth; ρp(*x*), predicted density of the lithospheric mantle as a function of *x*. These parameters are used to compute a mass balance expressed by equations (B1) and (B2).

and ZL(τ) in Figure A2a, and between ZL = 150 km (= LAB depth beneath a continent conducting a surface heat flow of 50 mW/m^2) and ZL(*Qs*) in Figure A2b.

[80] Information in Figure A2 was used to design the reference model and to select density values for the bodies forming the 3-D density model, as discussed in the main text.

Appendix B: Correcting the Density Structure of Oceanic Mantle Lithosphere

[81] Figure B1 represents, schematically and in a 2-D section, the relationship between the constant density of the oceanic mantle lithosphere selected for the forward gravity modeling ρ_M, the asthenospheric density ρ_A, the depth to the lithosphere-asthenosphere boundary (LAB) resulting from the forward modeling LAB_M (Figure 7a), the LAB depth predicted by a half-space cooling model LAB_P (Figure 7b) and the corrected density for the oceanic mantle lithosphere $\rho_\text{P}(x)$ that we want to calculate from the other parameters. The three latter magnitudes depend on the distance *x* from the trench axis.

[82] By construction of the 3-D density model, at $x = 0$ we have that $\text{LAB}_\text{M} = \text{LAB}_\text{P}$ and $\rho_\text{M} = \rho_\text{P}(x)$. For $x \neq 0$, a balance of the total mass contained in vertical columns of the modeled density structure and that expected for an age-dependent cooling model of the oceanic plate allows the following expression to be written

$$\rho_M[\text{LAB}_M - \text{ZM}] + \rho_A[\text{ZC} - \text{LAB}_M] = \rho_P(x)[\text{LAB}_P - \text{ZM}] + \rho_A[\text{ZC} - \text{LAB}_P] \qquad \text{(B1)}$$

where ZM is the depth to the oceanic Moho resulting from the gravity modeling (Figure 6a) and ZC is a compensation depth. Arranging this expression and considering the three-dimensional nature of the problem, we get

$$\rho_P(x,y) = \frac{\rho_M[\text{LAB}_M(x,y) - \text{ZM}(x,y)] + \rho_A[\text{LAB}_P(x,y) - \text{LAB}_M(x,y)]}{\text{LAB}_P(x,y) - \text{ZM}(x,y)} \qquad \text{(B2)}$$

where (*x*, *y*) denote the geographic coordinates of the evaluating point in a map. $\text{LAB}_\text{P}(x, y)$ (Figure 7b) was computed by the procedure discussed in Appendix A and considering the oceanic plate ages for the Nazca plate extracted from the grid of *Müller et al.* [1997]. This information was used together with the results of the 3-D density model for the depth to oceanic Moho ZM(*x*, *y*) (Figure 6a) and $\text{LAB}_\text{M}(x, y)$ (Figure 7a), and density values summarized in Table 1 for the lithospheric and sublithospheric oceanic mantle, to compute the corrected density values $\rho_\text{P}(x, y)$ from (B2) for each of the seven segments of the Nazca plate considered in this study (Figure 1a). The results of these calculations are shown in Figure 8.

[83] In order to test the validity of such a procedure, we modified the density structure of the 3-D model for the segment VII of the Nazca plate to coincide with that predicted by (B2). Figure B2 (top) shows a detail for one of the cross sections forming the segment VII in the original 3-D density model. Note the good fit between observed and modeled Bouguer anomaly and the similarity with the situation schematized in Figure B1, in particular that the mantle lithosphere is formed by one body of constant density, and that LAB_M and LAB_P diverge westward the trench axis. Figure B2 (bottom) shows the same cross section but with the mantle lithosphere has been divided in three different bodies according to the density values and distribution resulting for the proposed procedure and presented in Figure 8, segment VII. Using this corrected structure for the lithosphere, fixing the LAB depth to that predicted by the cooling model (LAB_P) and maintaining the rest of the density structure as defined initially by the 3-D density model, it can be observed that the fit between observed and modeled Bouguer anomaly remains as good as for the original situation in Figure B2 (top). This demonstrates that the procedure we use to compute cor-

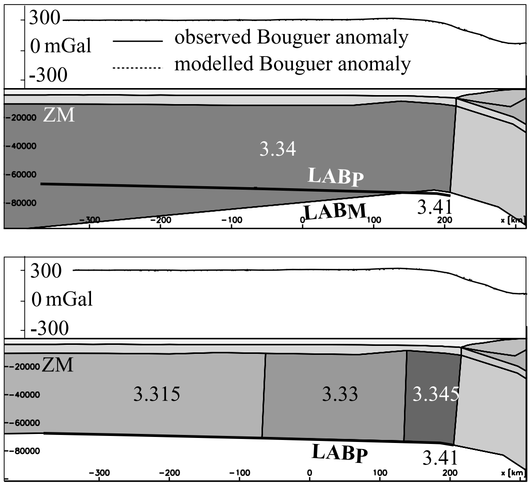

Figure B2. (top) part of a vertical cross section from the 3-D density model along segment VII of the Nazca plate. Note the good fit between observed and modeled Bouguer anomaly and the geometries and values of parameters defined in Figure B1. (bottom) Same cross section but with a lithospheric mantle structure corrected after applying the procedure of equation (B2). Note that the fit to the gravity field is as good as in Figure B2 (top).

rected densities for the oceanic mantle lithosphere is valid and generates a density structure that reproduces the gravity field.

[84] **Acknowledgments.** This project has been possible thanks to many colleagues in South America (Diana Comte, Mario Pardo, Jaime Campos, Denizar Blizkow), Europe (Sergio Barrientos, Tony Monfret, Antonio Villaseñor, Uwe Meyer, Ingo Wöbern), and United States (Robert Fromm), who provided us with original, mostly unpublished data. Daniel Melnick is especially thanked for his assistance with the GIS-based analysis of continental morphostructure. We benefited from fruitful discussions with Rick Allmendinger, Suzanne M. Kay, Stephen Kirby, Constantino Mpodozis, Onno Oncken, Victor Ramos, and Stephan Sobolev. This work was supported by the German Collaborative Research Center SFB267 "Deformation Processes in the Andes" funded by the Deutsche Forschungsgemeinschaft. A.T.'s Ph.D. project at the Freie Universität Berlin was supported by a scholarship from the German Academic Exchange Service (DAAD). We wish to acknowledge the useful comments and suggestions from the editor, Richard Arculus, the Associate Editor and two reviewers (who have preferred to remain anonymous).

References

Allmendinger, R. W., and T. Gubbels (1996), Pure and simple shear plateau uplift, Altiplano-Puna, Argentina and Bolivia, *Tectonophysics*, *259*, 1–13.

Allmendinger, R. W., T. E. Jordan, S. M. Kay, and B. L. Isacks (1997), The evolution of the Altiplano-Puna Plateau of the central Andes, *Annu. Rev. Earth Planet. Sci.*, *25*, 139–174.

Andersen, O. B., and P. Knudsen (1998), Global marine gravity field from the ERS-1 and GEOSAT geodetic mission altimetry, *J. Geophys. Res.*, *103*, 8129–8137.

Artemieva, I. M., and W. D. Mooney (2001), Thermal thickness and evolution of Precambrian lithosphere: A global study, *J. Geophys. Res.*, *106*, 16,387–16,414.

Bangs, N. L., and S. C. Cande (1997), Episodic development of a convergent margin inferred from structures and processes along the southern Chile margin, *Tectonics*, *16*, 489–503.

Barrientos, S., E. Vera, P. Alvarado, and T. Monfret (2004), Crustal seismicity in central Chile, *J. S. Am. Earth Sci.*, *16*, 759–768.

Beck, S., and G. Zandt (2002), The nature of orogenic crust in the central Andes, *J. Geophys. Res.*, *107*(B10), 2230, doi:10.1029/2000JB000124.

Beck, S., G. Zandt, S. Myers, T. Wallace, R. Silver, and L. Drake (1996), Crustal-thickness variations in the central Andes, *Geology*, *24*, 407–410.

Belmonte, A. (2002), Krustale Seismizität, Struktur und Rheologie der Oberplatte zwischen der Präkordillere und dem magmatischen Bogen in Nordchile (22°–24°S), Ph.D. thesis, 120 pp., Freie Univ. Berlin, Berlin, Germany.

Berrocal, J., Y. Marangoni, N. C. de Sá, R. Fuck, J. Soares, E. Dantas, F. Perosi, and C. Fernandes (2004), Deep seismic refraction and gravity crustal model and tectonic deformation in Tocantins Province, central Brazil, *Tectonophysics*, *388*, 187–199.

Bohm, M. (2004), 3-D Lokalbebentomographie der südlichen Anden zwischen 36° und 40°S, Ph.D. thesis, 130 pp., Freie Univ. Berlin, Berlin, Germany.

Bohm, M., S. Lüth, H. Echtler, G. Asch, K. Bataille, C. Bruhn, A. Rietbrock, and P. Wigger (2002), The southern Andes between 36° and 40°S latitude: Seismicity and average seismic velocities, *Tectonophysics*, *356*, 275–289.

Bonatti, E., C. G. A. Harrison, D. E. Fisher, J. Honnorez, J. G. Schilling, J. J. Stipp, and M. Zentilli (1977), Easter volcanic chain (south east Pacific): A mantle hot line, *J. Geophys. Res.*, *82*, 2457–2478.

Bown, J. W., and R. S. White (1994), Variation with spreading rate of oceanic crustal thickness and geochemistry, *Earth Planet. Sci. Lett.*, *121*, 435–449.

Breunig, M., A. B. Cremers, H.-J. Götze, R. Seidemann, S. Schmidt, S. Shumilov, and A. Siehl (2000), Geologic mapping based on 3D models using an interoperable GIS, *GIS J. Spatial Inf. Decis. Making*, *13*, 12–18.

Cahill, T., and B. Isacks (1992), Seismicity and shape of the subducted Nazca plate, *J. Geophys. Res.*, *97*, 17,503–17,529.

Campos, J., D. Hatzfeld, R. Madariaga, G. Lopéz, E. Kausel, A. Zollo, G. Iannacone, R. Fromm, S. Barrientos, and H. Lyon-Caen (2002), A seismological study of the 1835 seismic gap in south-central Chile, *Phys. Earth Planet. Inter.*, *132*, 177–195.

Carlson, R. (2004), Seismic properties of layer 2A at 11 Ma: Results of a vertical seismic profile at Ocean Drilling Program Site 1243, *Geophys. Res. Lett.*, *31*, L17601, doi:10.1029/2004GL020598.

Carlson, R. L., and D. J. Miller (2003), Mantle wedge water contents estimated from seismic velocities in partially serpentinized peridotites, *Geophys. Res. Lett.*, *30*(5), 1250, doi:10.1029/2002GL016600.

Carlson, R. L., and D. Miller (2004), Influence of pressure and mineralogy on seismic velocities in oceanic gabbros: Implications for the composition and state of the lower oceanic crust, *J. Geophys. Res.*, *109*, B09205, doi:10.1029/2003JB002699.

Carmichael, R. S. (1989), *Practical Handbook of Physical Properties of Rocks and Minerals*, CRC Press, Boca Raton, Fla.

Cembrano, J., F. Herve, and A. Lavenu (1996), The Liquiñe-Ofqui fault zone: A long-lived intra-arc fault system in southern Chile, *Tectonophysics*, *259*, 55–66.

Charrier, R., O. Baeza, S. Elgueta, J. Flynn, P. Gans, S. Kay, N. Muñoz, A. Wyss, and E. Zurita (2002), Evidence for Cenozoic extensional basin development and tectonic inversion south of the flat-slab segment, southern central Andes, Chile (33°–36°S.L.), *J. S. Am. Earth Sci.*, *15*, 117–139.

Chernicoff, C. J., and E. Zappettini (2003), Delimitación de los terrenos tectonoestratigráficos de la región centro-austral argentina: Evidencias aeromagnéticas, *Rev. Geol. Chile*, *30*, 299–316.

Christensen, N. I., and W. D. Mooney (1995), Seismic velocity structure and composition of the continental crust: A global view, *J. Geophys. Res.*, *100*, 9761–9788.

Clift, P. D., I. A. Pecher, N. Kukowski, and A. Hampel (2003), Tectonic erosion of the Peruvian forearc, Lima Basin, by subduction and Nazca Ridge collision, *Tectonics*, *22*(3), 1023, doi:10.1029/2002TC001386.

Cobbold, P. R., and E. Rossello (2003), Aptian to recent compressional deformation, foothills of the Neuquen Basin, Argentina, *Mar. Pet. Geol.*, *20*(5), 429–443.

Comte, D., H. Haessler, L. Dorbath, M. Pardo, T. Monfret, A. Lavenu, B. Pontoise, and Y. Hello (2002), Seismicity and stress distribution in the Copiapo, northern Chile subduction zone using combined on- and off-shore seismic observations, *Phys. Earth Planet. Inter.*, *132*, 197–217.

Comte, D., J. Battaglia, C. Thurber, H. Zhang, L. Dorbath, and B. Glass (2004), High-resolution subducting slab structure beneath northern Chile using the double-difference tomography method, *Eos Trans. AGU*, *85*(47), Fall Meet. Suppl., Abstract S53B-0200.

Creager, K. C., C. Ling Yun, J. P. Winchester, and E. R. Engdahl (1995), Membrane strain rates in the subducting plate beneath South America, *Geophys. Res. Lett.*, *22*, 2321–2324.

de Ignacio, C., I. Lopéz, R. Oyarzun, and A. Márquez (2001), The northern Patagonian Somuncura plateau basalts: A product of slab-induced, shallow asthenospheric upwelling, *Terra Nova*, *13*, 117–121.

Diraison, M., P. R. Cobbold, E. A. Rossello, and A. J. Amos (1998), Neogene dextral transpression due to oblique convergence across the Andes of northwestern Patagonia, Argentina, *J. S. Am. Earth Sci.*, *11*, 519–532.

Ebbing, J., E. Lundin, O. Olesen, and E. Hansen (2005), The mid-Norwegian margin: A discussion of crustal lineaments, mafic intrusions, and remnants of the Caledonian root by 3D density modelling and structural interpretation, *J. Geol. Soc.*, *163*, 47–59.

Engdahl, E. R., R. D. van der Hilst, and R. Buland (1998), Global teleseismic earthquake relocation with improved travel times and procedures for depth determination, *Bull. Seismol. Soc. Am.*, *88*, 722–743.

Feng, M., M. Assumpcao, and S. van der Lee (2004), Group-velocity tomography and lithospheric S-velocity structure of the South American continent, *Phys. Earth Planet. Inter.*, *147*, 315–331.

Flüh, E., N. Vidal, C. Ranero, A. Hojka, R. von Huene, J. Bialas, K. Hinz, D. Cordoba, J. Dañobeitia, and C. Zelt (1998), Seismic investigation of the continental margin off- and onshore Valparaiso, Chile, *Tectonophysics*, *288*, 251–263.

Folguera, A., D. Melnick, and V. A. Ramos (2002), Partición de la deformation en la zona del arco volcanico de los Andes neuquinos (36–39°S) en los úlitmos 30 millones de años, *Rev. Geol. Chile*, *29*, 227–240.

Folguera, A., V. A. Ramos, R. Hermanns, and J. Naranjo (2004), Neotectonics in the foothills of the southernmost central Andes (37°–38°S): Evidence of strike-slip displacement along the Antinir-Copahue fault zone, *Tectonics*, *23*, TC5008, doi:10.1029/2003TC001533.

Fromm, R., G. Zandt, and S. L. Beck (2004), Crustal thickness beneath the Andes and Sierras Pampeanas at 30°S inferred from Pn apparent phase velocities, *Geophys. Res. Lett.*, *31*, L06625, doi:10.1029/2003GL019231.

Gansser, A. (1973), Facts and theories on the Andes, *J. Geol. Soc. London*, *129*, 93–131.

Gerbault, M., J. Martinod, and G. Herail (2005), Possible orogeny-parallel lower crustal flow and thickening in the central Andes, *Tectonophysics*, *399*, 59–72, doi:10.1016/j.tecto.2004.12.015.

Godoy, E., G. Yáñez, and E. Vera (1999), Inversion of an Oligocene volcano-tectonic basin and uplifting of its superimposed Miocene magmatic arc in the Chilean central Andes: First seismic and gravity evidences, *Tectonophysics*, *306*, 217–236.

Götze, H.-J. (1984), Über den Einsatz interaktiver Computergraphik im Rahmen 3-dimensionaler Interpretationstechniken in Gravimetrie und Magnetik, Habil. Schrift, 236 pp., Tech. Univ. Clausthal, Clausthal-Zellerfeld, Germany.

Götze, H.-J., and B. Lahmeyer (1988), Application of three-dimensional interactive modeling in gravity and magnetics, *Geophysics*, *53*, 1096–1108.

Götze, H.-J., B. Meurers, S. Schmidt, and P. Steinhauser (1991), On the isostatic state of the eastern Alps and the central Andes: A statistical comparison, in *Andean Magmatism and Its Tectonic Setting*, edited by R. S. Harmon and C. W. Rapela, *Spec. Pap. Geol. Soc. Am.*, *265*, 279–290.

Götze, H.-J., B. Lahmeyer, S. Schmidt, and S. Strunk (1994), The lithospheric structure of the central Andes (20°–26°S) as inferred from quantitative interpretation of regional gravity, in *Tectonics of the Southern Central Andes*, edited by K.-J. Reutter, E. Scheuber, and P. J. Wigger, pp. 7–21, Springer, New York.

Gutscher, M.-A. (2002), Andean subduction styles and their effect on thermal structure and interplate coupling, *J. S. Am. Earth Sci.*, *15*, 3–10.

Gutscher, M.-A., W. Spakman, H. Bijwaard, and R. Engdahl (2000), Geodynamics of flat subduction: Seismicity and tomographic constraints from the Andean margin, *Tectonics*, *19*, 814–833.

Haberland, C., and A. Rietbrock (2001), Attenuation tomography in the western central Andes: A detailed insight into the structure of a magmatic arc, *J. Geophys. Res.*, *106*, 11,151–11,167.

Haberland, C., A. Rietbrock, B. Schurr, and H. Brasse (2003), Coincident anomalies of seismic attenuation and electrical resistivity beneath the southern Bolivian Altiplano plateau, *Geophys. Res. Lett.*, *30*(18), 1923, doi:10.1029/2003GL017492.

Hacker, B. R., and G. A. Abers (2004), Subduction factory: 3. An Excel worksheet and macro for calculating the densities, seismic wave speeds, and H_2O contents of minerals and rocks at pressure and temperature, *Geochem. Geophys. Geosyst.*, *5*, Q01005, doi:10.1029/2003GC000614.

Hacker, B. R., G. A. Abers, and S. M. Peacock (2003a), Subduction factory: 1. Theoretical mineralogy, density, seismic wave speeds, and H_2O content, *J. Geophys. Res.*, *108*(B1), 2029, doi:10.1029/2001JB001127.

Hacker, B. R., S. M. Peacock, G. A. Abers, and S. D. Holloway (2003b), Subduction factory: 2. Are intermediate-depth earthquakes in subducting slabs linked to metamorphic dehydration reactions?, *J. Geophys. Res.*, *108*(B1), 2030, doi:10.1029/2001JB001129.

Hamza, V. M., and M. Muñoz (1996), Heat flow map of South America, *Geothermics*, *25*, 599–646.

Henry, S. G., and H. Pollack (1988), Terrestrial heat flow above the Andean subduction zone in Bolivia and Peru, *J. Geophys. Res.*, *93*, 15,153–15,162.

Henstock, T., and P. Thompson (2004), Self-consistent modeling of crustal thickness at Chagos-Laccadive ridge from bathymetry and gravity data, *Earth Planet. Sci. Lett.*, *224*, 325–336.

Hervé, F. (1994), The southern Andes between 39° and 44°S latitude: The geological signature of a transpressive tectonic regime related to a magmatic arc, in *Tectonics of the Southern Central Andes*, edited by K.-J. Reutter, E. Scheuber, and P. J. Wigger, pp. 243–248, Springer, New York.

Hindle, D., J. Kley, O. Oncken, and S. Sobolev (2005), Crustal balance and crustal flux from shortening estimates in the central Andes, *Earth Planet. Sci. Lett.*, *230*, 113–124.

Husson, L., and T. Sempere (2003), Thickening the Altiplano crust by gravity-driven crustal channel flow, *Geophys. Res. Lett.*, *30*(5), 1243, doi:10.1029/2002GL016877.

Introcaso, A., M. C. Pacino, and H. Fraga (1992), Gravity, isostasy and Andean crustal shortening between latitudes 30° and 35°S, *Tectonophysics*, *205*, 31–48.

Isacks, B. (1988), Uplift of the central Andean plateau and bending of the Bolivian orocline, *J. Geophys. Res.*, *93*, 3211–3231.

Jacques, J. (2003), A tectonostratigraphic synthesis of the sub-Andean basins: Implications for the geotectonic segmentation of the Andean Belt, *J. Geol. Soc. London*, *160*, 687–701.

Jordan, T., B. L. Isacks, R. W. Allmendinger, J. Brewer, V. A. Ramos, and C. J. Ando (1983), Andean tectonics related to geometry of subducted Nazca Plate, *Geol. Soc. Am. Bull.*, *94*, 341–361.

Kay, R. W., and S. M. Kay (1993), Delamination and delamination magmatism, *Tectonophysics*, *219*, 177–189.

Kay, S., M. Gorring, and V. Ramos (2004), Magmatic sources, setting and causes of Eocene to Recent Patagonian plateau magmatism (36°S to 52°S latitude), *Rev. Asoc. Geol. Argent.*, *59*, 556–568.

Kendrick, E., M. Bevis, R. Smalley, B. Brooks, R. Barriga, E. Lauría, and L. Souto (2003), The Nazca–South America Euler vector and its rate of change, *J. S. Am. Earth Sci.*, *16*, 125–131.

Khazaradze, G., and J. Klotz (2003), Short- and long-term effects of GPS measured crustal deformation rates along the south central Andes, *J. Geophys. Res.*, *108*(B6), 2289, doi:10.1029/2002JB001879.

Kirby, S. H., E. R. Engdahl, and R. Denlinger (1996), Intermediate-depth intraslab earthquakes and arc volcanism as physical expressions of crustal and uppermost mantle metamorphism in subducting slabs, in *Subduction: Top to Bottom*, *Geophys. Monogr. Ser.*, vol. 96, edited by G. E. Bebout et al., pp. 195–214, AGU, Washington, D. C.

Kley, J., C. R. Monaldi, and J. A. Salfity (1999), Along-strike segmentation of the Andean foreland: Causes and consequences, *Tectonophysics*, *301*, 75–94.

Kopp, H., E. R. Flueh, C. Papenberg, and D. Klaeschen (2004), Seismic investigations of the O'Higgins Seamount Group and Juan Fernández Ridge: Aseismic ridge emplacement and lithosphere hydration, *Tectonics*, *23*, TC2009, doi:10.1029/2003TC001590.

Kozlovskaya, E., S. Elo, S. Hjelt, J. Yliniemi, M. Pirttijärvi, and SVEKALAPKO Seismic Tomography Working Group (2004), 3-D density model of the crust of southern and central Finland obtained from joint interpretation of SVEKALAPKO crustal P-wave velocity models and gravity data, *Geophys. J. Int.*, *158*, 827–848.

Krabbenhöft, A., J. Bialas, H. Kopp, N. Kukowsky, and C. Hübscher (2004), Crustal structure of the Peruvian continental margin from wide-angle seismic studies, *Geophys. J. Int.*, *159*, 749–764.

Krawczyk, C., and the SPOC Team (2003), Amphibious seismic survey images plate interface at 1960 Chile earthquake, *Eos Trans. AGU*, *84*(32), 301, 304–305.

Lamb, S. (2001), Vertical axis rotation in the Bolivian orocline, South America: 2. Kinematic and dynamical implications, *J. Geophys. Res.*, *106*, 26,633–26,653.

Lavenu, A., and J. Cembrano (1999), Compressional and tranpressional stress pattern for Pliocene and Quaternary brittle deformation in forearc and intraarc zones (Andes of central and southern Chile), *J. Struct. Geol.*, *21*, 1669–1691.

Lee, C.-T., A. Lenardic, C. Cooper, F. Niu, and A. Levander (2005), The role of chemical boundary layers in regulating the thickness of continental and oceanic thermal boundary layers, *Earth Planet. Sci. Lett.*, *230*, 379–395.

López-Escobar, L., J. Cembrano, and H. Moreno (1995), Geochemistry and tectonics of the Chilean southern Andes basaltic Quaternary volcanism (37–46°S), *Rev. Geol. Chile*, *22*, 219–234.

Lowry, A. R., N. M. Ribe, and R. B. Smith (2000), Dynamic elevation of the Cordillera, western United States, *J. Geophys. Res.*, *105*, 23,371–23,390.

Lucassen, F., R. Trumbull, G. Franz, C. Creixell, P. Vásquez, R. Romer, and O. Figueroa (2004), Distinguishing crustal recycling and juvenile additions at active continental margins: The Paleozoic to recent compositional evolution of the Chilean Pacific margin (36–41°S), *J. S. Am. Earth Sci.*, *17*, 103–119.

Lüth, S., P. Wigger, and ISSA 2000 Working Group (2003), A crustal model along 39°S from a seismic refraction profile—ISSA 2000, *Rev. Geol. Chile*, *30*, 83–101.

Marchenko, D. (2006), Geoid model for South America and surrounding oceans, Ph.D. dissertation, Univ. Potsdam, Potsdam, Germany, in press.

Mégard, F. (1984), The Andean orogenic period and its major structures in central and northern Peru, *J. Geol. Soc. London*, *141*, 893–900.

Mishra, D. C., K. Arora, and V. M. Tiwari (2004), Gravity anomalies and associated tectonic features over the Indian Peninsular Shield and adjoining ocean basins, *Tectonophysics*, *379*, 61–76.

Mpodozis, C., and V. A. Ramos (1989), The Andes of Chile and Argentina, in *Geology of the Andes and Its Relation to Hydrocarbon and Mineral Resources*, *Earth Sci. Ser.*, vol. 11, edited by G. Ericksen, M. Cañas Pinochet, and J. Reinemund, pp. 59–89, Circum-Pac. Res. Counc., Houston, Tex.

Müller, R. D., W. R. Roest, J.-Y. Royer, L. M. Gahagan, and J. G. Sclater (1997), Digital isochrons of the world's ocean floor, *J. Geophys. Res.*, *102*, 3211–3214.

Oleskevich, D. A., R. D. Hyndman, and K. Wang (1999), The updip and downdip limits to great subduction earthquakes: Thermal and structural models of Cascadia, south Alaska, SW Japan, and Chile, *J. Geophys. Res.*, *104*, 14,965–14,991.

Oncken, O., et al. (2003), Seismic imaging of a convergent continental margin and plateau in the central Andes (Andean Continental Research Project 1996 (ANCORP '96)), *J. Geophys. Res.*, *108*(B7), 2328, doi:10.1029/2002JB001771.

Pardo, M., D. Comte, and T. Monfret (2002), Seismotectonic and stress distribution in the central Chile subduction zone, *J. S. Am. Earth Sci.*, *15*, 11–22.

Pardo, M., T. Monfret, E. Vera, A. Eisenberg, and G. Yáñez (2003), Morfología de la subducción utilizando datos locales: Sismotectónica de Chile Central, paper presented at X Chilean Geologicla Congress, Concepcion, Chile.

Pardo-Casas, F., and P. Molnar (1987), Relative motion of the Nazca (Farallón) and South America plates since Late Cretaceous time, *Tectonics*, *6*, 233–248.

Peacock, S. M., and K. Wang (1999), Seismic consequences of warm versus cool subduction metamorphism: Examples from southwest and northeast Japan, *Science*, *286*, 937–939.

Pilger, R. (1984), Cenozoic plate kinematics, subduction and magmatism: South American Andes, *J. Geol. Soc. London*, *141*, 793–802.

Ramos, V. (1988), Tectonics of the late Proterozoic-early Paleozoic: A collisional history of southern South America, *Episodes*, *11*, 168–174.

Ramos, V. A., E. O. Cristallini, and D. J. Perez (2002), The Pampean flat-slab of the central Andes, *J. S. Am. Earth Sci.*, *15*, 59–78.

Regnier, M., J. Chiu, R. Smalley, B. Isacks, and M. Araujo (1994), Crustal thickness variation in the Andean foreland, Argentina, from converted waves, *Bull. Seismol. Soc. Am.*, *84*, 1097–1111.

Schmidt, S., and H.-J. Götze (1998), Interactive visualization and modification of 3D models using GIS functions, *Phys. Chem. Earth*, *23*, 289–296.

Schmitz, M., W. Heinsohn, and F. Schilling (1997), Seismic, gravity and petrological indications for partial melting beneath the thickened central Andean crust 21°–23°S, *Tectonophysics*, *270*, 313–326.

Schmitz, M., et al. (1999), The crustal structure of the central Andean forearc and magmatic arc as derived from seismic studies—The PISCO 94 experiment in northern Chile (21–23°S), *J. S. Am. Earth Sci.*, *12*, 237–260.

Schobbenhaus, C., and A. Bellizzia (2001), Geological map of South America, scale 1:5000000, Comm. for the Geol. Map of the World, Geol. Surv. of Brazil, Dep. Nac. da Produção Miner., UNESCO, Brasilia, Brazil.

Schurr, B., G. Asch, A. Rietbrock, R. Kind, M. Pardo, B. Heit, and T. Monfret (1999), Seismicity and average velocities beneath the Argentine Puna plateau, *Geophys. Res. Lett.*, *26*, 3025–3028.

Servicio Nacional de Geologia y Mineria (2003), Mapa geológico de Chile: Versión digital [CD-ROM], *Publ. Geol. Digital*, *4*, Santiago, Chile.

Servicio Nacional de Geológica Minero Argentina (1998), Mapa geológico de la Republica Argentina, Buenos Aires.

Sick, C., et al. (2006), Seismic images of accretive and erosive subduction processes from the Chilean margin, in *Subduction Orogeny Along the Andean Margin*, *Frontiers Earth Sci.*, vol. 1, edited by O. Oncken, Springer, New York, in press.

Simoes, M., J. P. Avouac, R. Cattin, and P. Henry (2004), The Sumatra subduction zone: A case for a locked fault zone extending into the mantle, *J. Geophys. Res.*, *109*, B10402, doi:10.1029/2003JB002958.

Sobolev, S., and A. Babeyko (1994), Modeling of mineralogical composition, density and elastic wave velocities in anhydrous magmatic rocks, *Surv. Geophys.*, *15*, 515–544.

Springer, M. (1999), Interpretation of heat-flow density in the central Andes, *Tectonophysics*, *306*, 377–395.

Springer, M., and A. Förster (1998), Heat-flow density across the central Andean subduction zone, *Tectonophysics*, *291*, 123–139.

Stern, C. (2004), Active Andean volcanism: Its geologic and tectonic setting, *Rev. Geol. Chile*, *31*, 161–206.

Tassara, A. (2005), Interaction between the Nazca and South American plates and formation of the Altiplano-Puna plateau: Review of a flexural analysis along the Andean margin (15°–34°S), *Tectonophysics*, *399*, 39–57.

Tassara, A. (2006), Factors controlling the crustal density structure underneath active continental margins with implications for their evolution, *Geochem. Geophys. Geosyst.*, *7*, Q01001, doi:10.1029/2005GC001040.

Tassara, A., and G. Yáñez (2003), Relación entre el espesor elástico de la litosfera y la segmentación tectónica del margen andino (15–47°S), *Rev. Geol. Chile*, *30*, 159–186.

Tebbens, S. F., and S. C. Cande (1997), Southeast Pacific tectonic evolution from early Oligocene to present, *J. Geophys. Res.*, *102*, 12,061–12,084.

Tichelaar, B. W., and L. J. Ruff (1991), Seismic coupling along the Chilean subduction zone, *J. Geophys. Res.*, *96*, 11,997–12,022.

Turcotte, D. L., and G. Schubert (2002), *Geodynamics*, Cambridge Univ. Press, New York.

van der Lee, S., D. James, and P. Silver (2001), Upper mantle S velocity structure of central and western South America, *J. Geophys. Res.*, *106*, 30,821–30,835.

van Hunen, J., A. van den Berg, and N. Vlaar (2004), Various mechanisms to induce present-day shallow flat subduction and implications for the younger Earth: A numerical parameter study, *Phys. Earth Planet. Inter.*, *146*, 179–194.

Vdovin, O., J. A. Rial, A. Levshin, and M. Ritzwoller (1999), Group-velocity tomography of South America and the surrounding oceans, *Geophys. J. Int.*, *136*, 324–340.

Villaseñor, A., W. Spakman, and E. R. Engdahl (2003), Influence of regional travel times in global tomographic models, *Geophys. Res. Abstr.*, *5*, Abstract A-08614.

von Gosen, W. (2003), Thrust tectonics in the North Patagonian Massif (Argentina): Implications for a Patagonia plate, *Tectonics*, *22*(1), 1005, doi:10.1029/2001TC901039.

Wagner, L. S., S. Beck, and G. Zandt (2005), Upper mantle structure in the south central Chilean subduction zone (30° to 36°S), *J. Geophys. Res.*, *110*, B01308, doi:10.1029/2004JB003238.

Watts, A. (2001), *Isostasy and Flexure of the Lithosphere*, Cambridge Univ. Press, New York.

Wessel, P., and W. Smith (1998), New, improved version of the Generic Mapping Tools released, *Eos Trans. AGU*, *79*, 579.

White, R. S., D. McKenzie, and R. O'Nions (1992), Oceanic crustal thickness from seismic measurements and rare earth element inversions, *J. Geophys. Res.*, *97*, 19,683–19,715.

Wigger, P., et al. (1994), Variation of the crustal structure of the southern central Andes deduced from seismic refraction investigations, in *Tectonics of the Southern Central Andes*, edited by K.-J. Reutter, E. Scheuber, and P. Wigger, pp. 23-48, Springer, New York.

Yáñez, G., and J. Cembrano (2004), Role of viscous plate coupling in the late Tertiary Andean tectonics, *J. Geophys. Res.*, *109*, B02407, doi:10.1029/2003JB002494.

Yáñez, G., C. R. Ranero, R. von Huene, and J. Díaz (2001), Magnetic anomaly interpretation across the southern central Andes (32°–34°): The role of the Juan Fernández Ridge in the late Tertiary evolution of the margin, *J. Geophys. Res.*, *106*, 6325–6345.

Yáñez, G., J. Cembrano, M. Pardo, C. Ranero, and D. Sellés (2002), The Challenger-Juan Fernández-Maipo major tectonic transition of the Nazca-Andean subduction system at 33–34°S: Geodynamic evidence and implications, *J. S. Am. Earth Sci.*, *15*, 23–38.

Yang, Y., M. Liu, and S. Stein (2003), A 3-D geodynamic model of lateral crustal flow during Andean mountain building, *Geophys. Res. Lett.*, *30*(21), 2093, doi:10.1029/2003GL018308.

Yuan, X., S. V. Sobolev, R. Kind, O. Oncken, and Andes Seismology Group (2000), New constraints on subduction and collision processes in the central Andes from comprehensive observations of P to S converted seismic phases, *Nature*, *408*, 958–961.

Yuan, X., S. Sobolev, and R. Kind (2002), Moho topography in the central Andes and its geodynamic implications, *Earth Planet. Sci. Lett.*, *199*, 389–402.

Yuan, X., G. Asch, K. Bataille, G. Bock, M. Bohm, H. Echtler, R. Kind, O. Oncken. and I. Wölbern (2006), Deep seismic images of the southern Andes, in *The Neuquen Andes*, edited by V. Ramos and S. Kay, *Spec. Pap. Geol. Soc. Am.*, in press.

Zeyen, H., P. Ayarza, M. Fernández, and A. Rimi (2005), Lithospheric structure under the western African-European plate boundary: A transect across the Atlas Mountains and the Gulf of Cadiz, *Tectonics*, *24*, TC2001, doi:10.1029/2004TC001639.

H.-J. Götze, R. Hackney, and S. Schmidt, Institut für Geowissenshaften, Christian-Albrechts-Universität zu Kiel, Otto-Hahn-Platz 1, D-24118 Kiel, Germany.

A. Tassara, Departamento de Geofísica, Facultad de Ciencias Físicas y Matemèticas, Universidad de Chile, Blanco Encalada 2002, Santiago, Chile. (andres@dgf.uchile.cl)